

Title: PKC ϵ controls the fusion of secretory vesicles in mast cells in a phosphatidic acid-dependent mode.

Authors: Emilio M. Serrano-López^{1†}, David López-Martínez^{1†}, Juan C. Gómez-Fernández^{1*}, Antonio Luis Egea-Jimenez^{2*} and Senena Corbalán-García^{1*}

Affiliations:

¹Department of Biochemistry and Molecular Biology A, Veterinary School, Universidad de Murcia, IMIB, CEIR Campus Mare Notrum (CMN), Campus Espinardo, 30100-Murcia, Spain.

²Centre de Recherche en Cancérologie de Marseille (CRCM), Equipe labellisée LIGUE 2018, Aix-Marseille Université, Marseille F-13284, France and Inserm U1068, Institut Paoli-Calmettes, and CNRS UMR7258, Marseille F-13009, France.

† These two authors contributed equally to the work.

* *Corresponding authors:*

Senena Corbalan-Garcia, Phone: +34 868884775. E-mail: senena@um.es

Antonio Luis Egea-Jimenez, Phone: +33 486977352. E-mail: antonio.egea@inserm.fr

Juan C. Gómez-Fernandez, Phone: +34 868884776. E mail: jcgomez@um.es

One Sentence Summary: Phosphatidic acid controls mast cells secretion.

Abstract:

PKC ϵ is highly expressed in mast cells and plays a fundamental role in the antigen-triggered activation of the allergic reaction. Although its regulation by diacylglycerols has been described, its regulation by acidic phospholipids and how this regulation leads to the control of downstream vesicle secretion is barely known. Here, we used structural and evolutionary studies to find the molecular mechanism that explains the selectivity of the C1B domain of PKC ϵ by Phosphatidic Acid (PA). This resided in a collection of Arg residues that form a specific rim on the outer surface of the C1B domain, around the diacylglycerol binding cleft. In RBL-2H3 cells, this *basic rim* allowed the kinase to respond specifically to phosphatidic acid signals that induced its translocation to the plasma membrane and subsequent activation. Further experiments in cells that overexpress PKC ϵ and a mutant of the PA binding site, showed that PA-dependent PKC ϵ activation increased vesicle degranulation in RBL-2H3 cells, and this correlated with increased SNAP23 phosphorylation. Over-expression of PKC ϵ in these cells also induced an increase in the number of docked vesicles containing SNAP23, when stimulated with PA. This accumulation could be attributed to the stabilizing effect of phosphorylation on the formation of the SNARE complex, which ultimately led to increased release of content in the presence of Ca²⁺ during the fusion process. Therefore, these findings reinforce the importance of PA signaling in the activation of PKC ϵ , which could be an important target to inhibit the exacerbated responses of these cells in the allergic reaction.

Introduction

Mast cells play an important role in allergy due to the activation of FcεRI by antigen-induced cross-linking of IgE-bound to the receptor (1). This activation initiates diverse signaling cascades resulting in the immediate release of pro-inflammatory agents (2). However, how these signals are regulated by the second messenger lipids generated upon activation remains unresolved. Phosphatidic acid (PA) has been recognized as a class of lipid messenger very important for mast cell function, and a decrease in its generation by PLD leads to a block in the translocation to membranes of several PKC isoenzymes, and to low levels of degranulation (3). PA production and degradation is highly controlled by the action of several enzymes including phospholipase D, diacylglycerol kinase, and PA-phosphatase among many others (4). To date, a wide number of proteins have been identified and characterized as PA-interacting proteins with a common feature in their binding motifs by sharing a collection of basic residues that interact with the negatively charged phosphate head group of the phospholipid (5).

Previous work in our lab has determined that PKCε exhibits a prominent affinity to interact with membranes enriched in phosphatidic acid and diacylglycerol through its C2 and C1B domains (6-9), suggesting a new pathway to control the function of this enzyme by membrane protein clustering. Further work in RBL-2H3 mast cells has demonstrated that both domains also exhibit a preferential affinity to localize at the plasma membrane in a PA-dependent manner (10, 11), indicating that PKCε might be a sensor for PA signalling at least in these cells. Although the 3D structure of the C2 domain in complex with PA has helped to define the aminoacidic residues involved in the membrane interaction (10), the lack of 3D structure for the C1B domain or the full-length enzyme have hampered a complete study to find the molecular mechanism for membrane

interaction and consequent activation of this isoenzyme. Furthermore, how this PA-dependent activation of PKC ϵ transduces to downstream targets is still unknown.

Mast cells mainly secrete their mediators by degranulation of cytosolic granules or through carrier vesicles emanating from the Golgi. Studies using knock-out mice and siRNA experiments have demonstrated that the main SNARE complex driving RBL-2H3 cells degranulation is formed by SNAP23/STX4/VAMP8 (12). However, how this process is regulated at the molecular level is still not well defined. The proteins integrating the SNARE complex contain sequences that are potential sites for post-translational modifications like phosphorylation. For example, phosphorylation of SNAP23 (S95 and S120) is an important event in the regulation of vesicle fusion and secretion by controlling SNAP23 localization in the plasma membrane and internal membranes (13). However, the lack in 3D structure of the full-length complex impedes to figure out how phosphorylation might promote the SNARE complex function. A recent phosphoproteomic analysis has identified that phosphorylation of VAMP8 by PKC β suppresses secretion in mast cells but still permits docking (14), pointing the PKC family as important elements in the control of mast cells secretion. At least five PKC isoenzymes have been identified (α , β , δ , ϵ and ζ) in mast cells (15). Many studies indicate that PKC α and β are involved in degranulation and IL-6 production in RBL-2H3 cells (16, 17). Other works using knock-out mice show that PKC β and ϵ activation induces *c-fos* and *c-jun* expression (18). Furthermore, PKC α and θ promote IL-6 secretion following antigen stimulation and this is counter-regulated by PKC β and ϵ in bone marrow-derived mast cells (19).

Given the lack of information into the PA signal transduction in these cells and our previous results, we examined the signaling underlying PKC ϵ in a PA/DAG-dependent mode. We focused on determining the aminoacidic residues in the C1B domain responsible for PA interaction with

the plasma membrane and how this might affect to the subcellular localization of the proteins forming the SNARE complex that are responsible for vesicle secretion in RBL-2H3 mast cells. Therefore, we speculated that PA induces an increase of vesicle release that is dependent on PKC ϵ -dependent phosphorylation of at least, SNAP23 at the plasma membrane, probably leading to a more stable formation of the docking complexes that results in an enhancement of degranulation in the presence of Ca²⁺.

Results

Structural characterization of the C1B domain of PKC ϵ identifies a specific basic rim around the diacylglycerol binding cleft

To search for the aminoacidic residues involved in the PA interaction, we modelled the 3D structure of the C1B domain of PKC ϵ with Phyre2 (20) and docked a 1,2-diacetyl-*sn*-glycerol molecule in the diacylglycerol binding pocket by using SwissDock (21). The results showed the typical 3D structure of a C1B domain with two long β -sheets forming a V-shaped activator binding groove and a short α -helix at the C-terminal end (Fig. 1A). Folding was stabilized by the conserved two sets of three C and one H that can form two Zn²⁺ ion coordination sites at the end of the β -sheets (22, 23). The activator binding groove of C1B ϵ was formed by T254, L262, and L263 at the bottom cleft and V252, P253, G265, L266 and L267 at the top of the hydrophobic cleft. Strikingly, M239 in the C1B δ domain is substituted by a K residue in the C1B ϵ domain (Fig. 1B). Docking of the 1,2-diacetyl-*sn*-glycerol rendered 256 poses grouped in 48 clusters, most of them fitted into the diacylglycerol binding pocket (Fig. 1A). Basically, the top-ranked poses bind through hydrophobic interactions and they only establish a maximum of two hydrogen bonds through the OH at the C3 and/or the C=O groups of the C1 and C2 of the glycerol backbone (Fig.

1C). The lower number of hydrogen bonding, together with a lack in the hydrophobicity of the cleft, support the lower affinity binding described for 1,2-diacylglycerol in biochemical assays (24) and the higher affinity for PA-containing membranes when comparing the C1B ϵ with the C1B δ domains (11).

To get further insights into the molecular mechanism that could facilitate the interaction of this C1B ϵ domain into the membrane, we compared the electrostatic potentials of the C1B ϵ and C1B δ (PDB: 1PTR, (23)) domains calculated by using APBS (Fig. 1D, E). The C1B ϵ features a large electropositive surface surrounding the top of the diacylglycerol binding cleft, forming a basic rim with the contribution of the side chains of K251/R268/R282/R283. However, the C1B δ exhibits a smaller electropositive surface centered at the K256/H270/K271 residues (compare bottom views of Fig. 1D, E), suggesting that the larger electropositive potential in PKC ϵ , together with the length and conformations of the R residues might contribute to the higher affinity of this domain to interact with PA-enriched membranes. Primary sequence alignment of these residues confirms the results obtained by the 3D structures, indicating that K251/R268/R282/R283 in C1B ϵ could be potential candidates to interact with negatively charged phospholipids at the plasma membrane (Fig. 1B).

Thus, we used the Orientation of Proteins in Membranes server (25) to dock the C1B ϵ domain into a modeled membrane bilayer. Fig. 2A shows a binding mode where the basic residues identified are interacting with the membrane-water interface while the diacylglycerol molecule sits into the hydrophobic part of the lipid bilayer. To explore the evolutionary conservation of these amino acids, we studied the individual amino acids of the C1B ϵ domain by using ConSurf (26). The scores calculated rendered the K and R residues belonging to the rim as variable positions (Fig. 2B), showing that these residues might evolve to fit the PA-interacting specific function of

this C1B domain of PKC ϵ while keeping intact the conserved functional/structural positions (Fig. 2B).

Previous work from our laboratory has shown that the C1B domain of PKC ϵ and η have similar binding affinities to PA (11). Primary sequence alignment showed that three of the residues are conserved in C1B η with the exception of R282 in C1B ϵ that is substituted by I285 in C1B η , suggesting that a combination of 2Arg-1Lys in the basic rim might be sufficient to establish interactions with PA at the membrane (Fig. 2C). We also observed that among the variable regions in C1B ϵ , located about 12 Å of the basic rim, there are two K residues (K274 and K277) that are conserved in the C1B η domain (K277 and K280) (Fig. 2B, C) providing an additional electropositive surface that, although not directly interacting with the membrane, could contribute to the stabilization of the domain's interaction with membrane PA (Fig. 2D). In contrast, these two residues are not conserved in the C1B δ (PDB: 1PTR) and θ (PDB: 4FKD) and are replaced by E262, G265 in C1B δ and by D263, G266 in C1B θ , providing an electronegative surface instead. Furthermore, when the overall 3D structures are compared, ϵ and η have a broader electropositive rim formed by the side chains of the four residues (Fig. 2D). In contrast, δ and θ do not form this basic rim and the side chains of the residues are separated into two sets, suggesting that the lower affinity exhibited is due to a combination of less favoured 3D distribution of the key residues and the net charge provided by them (Fig. 2 C, D).

Taken together, this structural analysis suggests the existence of a specific *basic rim* located on the top surface of the C1B ϵ and η domains that could be responsible for its selectivity for PA.

Characterization of the PA-dependent interaction and activation of PKC ϵ in RBL-2H3 cells

To study the role of these amino acids in the membrane targeting of the C1B ϵ domain, K/R residues were mutated to the hydrophobic residue A. Single, double and triple C1B ϵ -ECFP mutants were expressed in RBL-2H3 mast cells and then, stimulated with antigen (DNP-HSA) or with different concentrations of 1,2-dioctanoyl-*sn*-phosphatidic acid (DOcPA) and/or 1,2-dioctanoylglycerol (DOcG) (Table S1). Spatio-temporal localization of the domain was studied by using confocal microscopy in time-lapse experiments. Thus, we measured three parameters: number of cells responding to stimulation with plasma membrane localization (M.L.), maximal relative increase in plasma membrane localization (R_{\max}), and half-time of translocation ($t_{1/2}$). Only 50% of the cells expressing single mutants showed their plasma membrane localization upon DNP-HSA stimulation compared with the 80% of cells expressing the WT domain (Table S1). However, of the cells that responded, only a small significant decrease in the percentage of protein localized at the plasma membrane was observed, with the R283A mutant being the most affected (33%) (Fig. S1A, B). Similar results were detected with a combination of DOcPA and DOcG (Fig. S1C). The mutants also showed a significant delay in the half-time of translocation ($t_{1/2}$), being R283A the most harmful mutation (Fig. S1D, E). Independent stimulations either with DOcPA or DOcG were not able to get the same localization parameters than a combination of both, confirming that both signals are needed to get a proper localization of the domain (Table S1). In spite of having a high hydrophobic potential, no plasma membrane localization was observed for double and triple mutants under similar conditions (Table S1), suggesting that the electropositive rim is playing a crucial role in the PA-dependent membrane docking of the domain in addition to the interaction with diacylglycerol.

To confirm this PA-dependent interaction, we used cell lysates from HEK293 cells expressing WT and mutants C1B ϵ -ECFP domain and measured their ability to interact with increasing concentrations of lipid vesicles containing POPC/POPA/OGPE (molar ratio 75:20:5) in the absence of DOG. Point mutations of the basic residues affected the affinity and percentage of mutants anchored to membranes. This effect increased with the number of A substitutions in the electropositive rim, being the K268A/R282A/R283A the most damaging (Table S2). As expected, the inclusion of 5 mol% of DOG in the lipid vesicles recovered the binding affinity of the mutants partially (Table S2). Together, these results show that hydrophobic conversion of the K/R residues at the rim, dramatically impairs the ability of the C1B ϵ domain to interact with PA and, suggests that the presence of this electropositive potential supported by these basic residues is critical to enable the domain to interact with PA, despite keeping intact the DOG-binding pocket.

To test whether the change in these two amino acids could be the reason for the differential affinity of C1B ϵ and C1B δ for PA, we mutated K251 and R282 in C1B ϵ to M and H, respectively (C1B ϵ K251M/R282H-ECFP). The C1B ϵ K251M/R282H-ECFP mutant showed significant decreases of 3.7-fold in maximal binding and 15.5-fold in affinity to POPA-containing vesicles, which persisted in the presence of DOG (Table S2). These parameters were very similar to those calculated for the wild-type C1B δ domain in previous work [in the absence of DOG: % maximal binding of 0.26 ± 0.02 and a K_D of 43.65 ± 0.79 μ M and maximal binding of 0.21 ± 0.05 % and a K_D of 20.4 ± 0.83 μ M in the presence of DOG] (11). In addition, transient expression of the C1B ϵ K251M/R282H-ECFP mutant in RBL-2H3 cells showed a significant decrease in the number of cells responding to antigen stimulation (60%) or additions of DOcPA and DOcG (63%) (Table S1) and consequently, the reduction of both half-time and plasma membrane localization was lower than those measured for the C1B δ -ECFP domain previously (11). Together, they confirm

that the integrity of the basic rim is essential to confer the C1B ϵ domain its ability to interact with PA-containing membranes and reveal the specific component of the K/R residues that compose the basic rim in the upper surface of this domain.

Given that previous work has demonstrated the role of the C2 domain of PKC ϵ in the membrane localization of the enzyme (10), we also investigated the role of the basic motif of the C1B domain in the membrane localization of full-length PKC ϵ . We generated single (PKC ϵ K251A-EGFP and PKC ϵ R268A-EGFP) (Fig. 3A) and double mutants (PKC ϵ R282A/R283A-EGFP) that were transfected in RBL-2H3 cells. Single mutations exhibited a 30% inhibition on the percentage of membrane anchored to membrane (R_{max}) upon antigen stimulation (Fig. 3B). This inhibition was not recovered by additions of exogenous DOcPA or DOcG or combinations of both (Table S3). Double mutation of residues R282/R283 to A produced a more drastic effect on protein localization, in only 68% of the transfected cells, the mutant protein translocated partially to the plasma membrane with a slower rate (55% inhibition in its R_{max} and 2.6-fold decrease in $t_{1/2}$ see Fig. 3B, C and Table S3). The inability of this mutant to interact with the plasma membrane persisted after additions of DOcPA or DOcG (Fig. S2A, B). To further block the interaction between positively charged amino acidic residues in the C1B ϵ domain and the plasma membrane, a quadruple mutant construct (PKC ϵ K251A/R268A/R282A/R283A-EGFP: PKC ϵ -4MUT-EGFP) was prepared and no detectable translocation was observed when the same concentrations of DOcPA and DOcG and their combinations were used (Table S3).

A conclusion that could be drawn from these results is the key role of the C1B domain for the membrane translocation of PKC ϵ through a specific interaction with PA at the membrane.

We also studied the role of the basic rim in the PA-dependent activation of PKC ϵ by comparing the catalytic activity of wild type PKC ϵ -WT-EGFP and the mutant PKC ϵ -4MUT-EGFP

at different percentages of POPA in the membranes in the absence or presence of DOG (Fig. 3D). It is interesting to note that no basal specific activity was detected when the phospholipid vesicles contained 5 mol% DOG in the absence of POPA, but it was necessary to include DOG into the lipid vesicles to observe a POPA-dependent activation (Fig. 3D). However, the basic rim mutant showed a drastic inhibition (77%) of the catalytic activity compared with the wild-type kinase. Together, these results indicate that both POPA and DOG are necessary for full activation of the enzyme and reinforce the idea that both lipids might coexist in microdomains at the plasma membrane to induce a proper localization and activation of the kinase.

PA-dependent activation of PKC ϵ enhances phosphorylation of the SNARE complex and further secretion in RBL-2H3 cells.

To explore the role of PA-dependent activation of PKC ϵ in RBL-2H3 cells degranulation, we generated stable cell lines overexpressing PKC ϵ -WT-EGFP and PKC ϵ -4MUT-EGFP (Fig. S3). Fc ϵ RI cross-linking leads to the activation of several signaling pathways that induce hydrolysis of PIP₂ in the DAG that remains on the membrane and IP₃ that induces release of Ca²⁺ from the internal stores and consequent mast cell degranulation. Due to this complex signaling, it is difficult to discern the molecular control mechanisms for a given protein, mainly when this protein is not activated by Ca²⁺ as is the case with PKC ϵ .

To study the individual effect of PA-dependent PKC ϵ activation on vesicle secretion independently of Ca²⁺, we first stimulated the cells with cell permeable PA and DOG, i.e. DOcPA or a combination of DOcPA/DOcG for 5 min and observed the release rate of β -hexosaminidase. No release was measured under these conditions when compared to non-stimulated cells (Fig. 4A). Only, when an influx of Ca²⁺ was induced by ionomycin, the release of β -hexosaminidase

increased to 35% in mock cells and to 43% in the cells expressing PKC ϵ -WT-EGFP and 37% in the cells expressing PKC ϵ -4MUT-EGFP (Fig. 4A). This indicates that the location of PKC ϵ in the plasma membrane facilitates the release process, probably acting in the pre-fusion state.

Then, we studied the effect of PA-dependent PKC ϵ activation on phosphorylation of SNARE machinery components which, in RBL-2H3 cells are mainly SNAP23, STX4 and VAMP8 (12). Fig. 4B shows the results obtained for the phosphorylation-induced mobility shift of SNAP23 in a 17% SDS-PAGE followed by WB (27). WB quantification shows the tendency to increase the amount of phosphorylated SNAP23 by stimulating cells that express PKC ϵ -WT-EGFP with DOcPA/DOcG (Fig. 4C). However, this is not the case of cells expressing PKC ϵ -4MUT-EGFP that do not respond to this stimulation with a phosphorylation-induced mobility shift, suggesting that PKC ϵ could control the specific phosphorylation of SNAP23 before Ca²⁺ activates vesicle fusion and content release. No change in electrophoretic mobility shift was observed for STX4 and VAMP8 (Fig. S4), although we cannot rule out that they may be phosphorylated at sites that do not induce this effect in electrophoresis.

To test how PA-dependent activation of PKC ϵ could affect the subcellular location and function of each one of the SNARE complex components, we induced the translocation of the kinase to the plasma membrane by addition of DOcPA+DOcG for 5 min and each one of the proteins, i.e., SNAP23, STX4 or VAMP8 were independently immunostained and characterized by two-color TIRF microscopy imaging. TIRF imaging can identify single secretory granules within <100 nm from underneath the plasma membrane and it is a very useful tool to explore the docking and fusion events (28).

We first explored by TIRF the plasma membrane localization of PKC ϵ -WT-EGFP upon PA-stimulation and demonstrated that PKC ϵ localizes to microdomains in the plasma membrane

(Fig. S5A) when cells are stimulated with DOcPA/DOcG (Fig. S5B, C). However, when the cells expressing PKC ϵ -4MUT were analyzed, we observed that the localization in microdomains in the plasma membrane was less defined and the amplitude of the fluorescence intensity did not increase with stimulation (Fig. S5A, B, C) confirming the inability of the mutant to respond to PA signals at the membrane.

When immunofluorescences of SNAP23 were analyzed by TIRF, they revealed a vesicular pattern (puncta) distributed across the plasma membrane that is attributed to different classes of docked secretory granules (SGs) carrying SNAP23 (29) (Fig. 5A). We measured the number of SGs (puncta) containing SNAP23 before and after the addition of DOcPA/DOcG and observed a significant increase when stimulating cells expressing PKC ϵ -WT-EGFP (Fig. 5B). Strikingly, cell expressing PKC ϵ -4MUT showed a similar number of puncta than stimulated PKC ϵ -WT but they did not respond to DOcPA/DOcG stimulation (Fig. 5B). These results indicate that PA-dependent activation of PKC ϵ could act by increasing the number of vesicles attached to the plasma membrane, thus favoring the release of contents when intracellular calcium increases. The already high number of steady-state vesicles in the case of the mutant precisely indicates the accumulation due to the lower release rate and lack of response to PA stimulation.

VAMP8-specific immunofluorescence TIRF images also showed a typical pattern of plasma membrane-docked vesicles (Fig. 6A). The number of puncta did not increase in cells expressing PKC ϵ -WT when stimulated with DOcPA/DOcG (Fig. 6B) nor in cells expressing PKC ϵ -4MUT, indicating that PA-dependent PKC ϵ activation does not affect this set of vesicles.

TIRF imaging of STX4-specific immunofluorescence showed very similar results to those of VAMP8 in PKC ϵ -WT-expressing cells (Fig. 6C). However, cells expressing PKC ϵ -4MUT

showed a significant decrease in the number of docked vesicles when stimulated with DOcPA/DOcG (Fig. 6C, D), suggesting a slightly inhibitory effect independent of PKC ϵ .

Taken together, these results demonstrate that PA-dependent PKC ϵ activation in RBL-2H3 cells is responsible for the accumulation of docked SGs containing SNAP23 at the plasma membrane when cells are activated by DOcPA/DOcG. This stimulation results in a translocation of the kinase to the plasma membrane leading to phosphorylation of at least SNAP23. This phosphorylation event likely serves to prime the docked vesicles for a more effective vesicle fusion and release of contents when Ca²⁺ pulses occur.

Discussion

Given the importance of mast cells in the control of allergy, autoimmunity, cardiovascular diseases, and cancer, it is important to figure out how these cells modulate their differential responses to be able to develop specific therapeutic applications. After many years of work, there is still a big lack of information about the molecular mechanisms that control the interface between signaling at the cell surface and the exocytic fusion machinery. PKCs are among the key players in the signal transduction pathways in mast cells, as they can detect many different signaling lipids in the plasma membrane. Nevertheless, how each individual isoenzyme connects and controls the vesicle secretion system is still under study. We therefore sought to combine structural with biochemical and living cell analyses to elucidate the signaling underlying PA activation of PKC ϵ and how this specific lipid signaling can control the process of vesicle fusion for degranulation at the plasma membrane of RBL-2H3 mast cells.

The basic rim of the C1B domain of PKC ϵ controls the PA-dependent membrane interaction and activation in RBL-2H3 cells

The lack of the high-resolution structure of the C1-DAG complex in PKCs has impeded us to pinpoint the structural determinants that cause the different affinities of these isoenzymes for PA. In the present study, a 3D structure of the C1B domain of PKC ϵ was predicted by homology modelling and the electrostatic potential distributions on the surface was calculated and compared with that of the C1B domain of PKC δ . Strikingly, the C1B ϵ domain exhibited a large predominant positive electrostatic potential conferred by a collection of K and R residues forming a basic rim on top of the domain. This electrostatic rim is partially conserved in the C1B δ domain and the presence of M239 in one of the edges of the rim dramatically decreases the electropositive surface available to interact with membranes.

The conservation profile calculated by ConSurf demonstrates that the C1B domain is highly conserved in its structural determinants and in the residues forming the ligand binding cleft. Lower conservation is observed in the areas at the outer side of the domain where the *basic rim* is located. Primary sequence alignment of the C1A and C1B domains of the different PKC isoenzymes reveals that the complete *basic rim* is unique in the C1B ϵ domain (see (30) for alignment), only the C1A ϵ and the C1A η and C1A γ conserve the four basic residues. Molecular dynamics simulations comparing K and R residues have demonstrated that R possesses a unique ability to form extensive H-bonds with phosphate groups of lipids, which leads to enhanced membrane interfacial binding (31), this implies that although a substitution of an R residue for a K can be considered conservative, in this molecular mechanism this substitution can make strong differences. Additional support has been found by comparing the 3D structures of the C1B domains of PKC ϵ and η that have similar binding affinities to PA and those of PKC δ and θ that show lower binding affinities for this acidic lipid (11). Fig. 2D clearly shows how the *basic rim* only appears in the 3D structure of C1B ϵ and η and yet C1B δ and θ do not form the typical rim

despite having at least three basic residues. In addition, other sites in ϵ and η further away from the contact surface could also influence the affinity as they provide a more electropositive surface. These findings are very relevant due to the important significance they have in explaining the differential behaviour of the different isoenzymes, and which lies in a very sophisticated molecular mechanism that has no answer to the mere exploration of the primary sequence alignment and has required a more complex combination of 3D structure and surface electrostatic studies.

Taken together, these results suggest that the combination of 3-4 basic residues in C1B ϵ and η and the formation of a specific *basic rim* together with a combination of basic residues at a distal site of the domain provide a very large electropositive area and are essential for establishing a specific H-bond network that better anchors the domain in the appropriate position with respect to the lipid-water interface in PA-enriched microdomains.

The results obtained in RBL-2H3 cells in this work confirm this hypothesis, we observed that an increase in the number of mutations to A at the *basic rim* correlates with the inability of both the domain and full-length protein to translocate to the plasma membrane. This strengthens the hypothesis of a membrane interaction driven by the specific R residues, otherwise we would observe no effect or enhanced binding due to the increase in the hydrophobic components of the site. Furthermore, the intend to mutate key residues like K251 to M and R282 to H to convert the sequence of the C1B ϵ domain into C1B δ , rendered a damaging effect as well, supporting the idea that these residues are essential for the PA selectivity of PKC ϵ (9, 11, 24). The results obtained in previous studies by mutating the hydrophobic residues located at the *top rim* of the ligand binding cleft in the C1B δ domain to hydrophilic residues showed that the domain experimented a large reduction in its binding affinity to DAG and became more dependent of negatively charged phospholipids to interact with membranes (32). Although, the main aim of this work was to

demonstrate the role of these residues for DAG interaction, it was showing indirectly that an equilibrium between internal hydrophobic and external hydrophilic residues on the top part of the C1 domains form a very intricate system to fine tune the affinities for DAG and negatively charged phospholipids of the different PKC isoenzymes.

The harmful effect obtained by introducing the four mutations to A in the catalytic activity of PKC ϵ indicate that this membrane interaction is also important to get access to the substrate, note how in the presence of only DAG in membranes and total absence of PA, no catalytic activity was measured, indicating that in spite of being able to interact with membranes in a DAG-dependent mode, it is not possible to get full activation till the C1B domain establishes the electrostatic interactions with the PA-containing membranes.

Previous studies have described the molecular mechanism by which the C2 domain of PKC ϵ interact with PA. Mutations abolishing the PA-binding site inhibited the ability of the enzyme to interact with the plasma membrane that was recovered by an excess of DAG (10). A comparative study has also reported that the C2 domains of PKC ϵ and PKC δ contribute partially to the membrane binding affinity of these enzymes (24), being PKC ϵ the one exhibiting a higher selectivity for PA-containing membranes.

The results obtained in the present work demonstrate that mutations at the *basic rim* in the C1B domain are more deleterious than those at the C2 domain, and they cannot be recovered by an excess of DAG, pointing to a model in which C1 and C2 domains cooperate to position the enzyme in PA/DAG enriched areas of the plasma membrane.

Phosphatidic Acid-dependent activation of PKC ϵ enhances mast cell secretion by phosphorylation of the SNARE complex in a docking step.

Our data show that PA-dependent activation of PKC ϵ increases RBL-2H3 cell secretion and this might be related to SNAP23 phosphorylation. The localization studies of SNAP23, STX4 and VAMP8 in RBL-2H3 cells indicate that the PA-dependent activation of PKC ϵ has different effects on the individual components of the SNARE complex.

The increased accumulation of SNAP23-containing vesicles near the plasma membrane of cells activated with PA suggests that SNAP23 phosphorylation may be inducing a blockage of pre-fusion steps (docking and priming) (Fig. 5). Since increased release of contents is observed in the vesicles of cells expressing PKC ϵ -WT (Fig. 4A), it is more likely that SNAP23 phosphorylation is stabilizing and increasing the number of docking events to prepare the vesicles for effective release in the presence of Ca²⁺. This hypothesis would also explain why the number of SGs increases in cells that express PKC ϵ -4MUT but nevertheless do not respond to PA/DOG stimulation, since in this case, there would be an effective blockade in the pre-fusion state due to the lack of phosphorylation that cannot be overcome by the presence of Ca²⁺.

This observation is very similar to the effect found in a previous work showing that IKK2 phosphorylation stimulates the exocytic pathway in mast cells (29). This study demonstrated that plasma membrane association of SNAP23 was controlled by T102 constitutive phosphorylation. Additional induced phosphorylation at S95 and S120 was responsible for the relocation of SNAP23 to different pools of secretory granules (29). Similarly, in our study, a PKC ϵ -dependent phosphorylation of SNAP23 by endogenous PA signaling may be responsible for the location of the protein in docked vesicles and would explain why cells expressing PKC ϵ -WT exhibited higher secretion than those expressing PKC ϵ -4MUT.

Localization experiments of vesicles containing STX4 or VAMP8 showed very similar results and no effect was observed when cells were stimulated with PA/DOG, suggesting that PA-dependent PKC ϵ activation is not responsible for VAMP8 and STX4 phosphorylation, or at least if this occurs it is not affecting docking and priming events.

No PKC-dependent phosphorylation of STX4 has been described to date. Moreover, PKC β -dependent phosphorylation of VAMP8 has demonstrated a reduction in degranulation from RBL-2H3 cells, owing to an stabilization of the vesicle docking step (14). This scenario indicates that it is highly possible that PKC ϵ uses the PA signaling pathway to exert a specific phosphorylation over SNAP23 and this combines with phosphorylation of other SNARE components by other PKC isoenzymes leading to an stabilization of the docking step in vesicle fusion to enhance degranulation in RBL-2H3 cells. How phosphorylation influences the complex at the molecular level is difficult to predict since no 3D structural or biological information are available. In a detailed exploration of the PhosphositePlus database (33) to find the most frequent phosphosites identified by mass spectrometry for SNAP23, STX4 and VAMP8 (Table S4), we found that VAMP8 and SNAP23 proteins contain phosphorylation sites that are located in the coiled-coil SNARE structure and the rest of the phosphorylation sites reside outside this domain. We tried to model the 3D structure of the coiled-coil SNARE complex formed by SNAP23, VAMP8 and STX4 (Fig. 7A). The structure modelled show how layer 0 in the coiled-coil is arranged by conserved residues VAMP8R36, STX4E230, SNAP23Q40 and SNAP23Q179 of the SNARE complex and it is stabilized by hydrogen bonds (Fig. 7B). When we focused on the residues of SNAP23 and VAMP8 that could be potentially phosphorylated by PKC ϵ and PKC β , respectively (Fig. 7A), we observed that most of the SNAP23 sites reside in the linker connecting the N and C-terminal helices that form the SNARE complex. In addition, two more areas are

affected by phosphorylation at the SNARE complex, one at its C-terminal (Fig. 7C) with phospho potential residues of VAMP8 that are participating in H-bonding at the inside face of the coiled-coil. The second area is located at the N-terminal of the SNARE complex and is formed by potential phosphorylation sites of SNAP23 and VAMP8 with the difference that the side chains of these residues point to the outside face of the coiled-coil (Fig. 7D).

Based on our findings, we show a structural model for a new site in the C1B domain of PKC ϵ that is specific for PA signaling in RBL-2H3 cells. We hypothesize that this lipid-protein specific interaction locates the kinase in the proper orientation at the membranes to activate and connect with the SNARE fusion machinery. Evidence is suggesting that PA-activation of PKC ϵ at the plasma membrane directly controls SNAP23 phosphorylation. The role of phosphorylation of some residues in the SNARE complex might be to stabilize the coiled-coil structure during the docking/priming of the vesicles and therefore enhancing the proportion of the secretion process in the presence of Ca²⁺. Further work needs to be done to precisely determine the specific PKC ϵ phosphorylation sites in SNAP23, how activation of PKC ϵ affects directly or indirectly VAMP8 and STX4 and the complete signaling pathways controlled by this specific activation of PKC ϵ dependent of PA to exploit its potential therapeutic applications.

Materials and Methods

Materials

All lipids were obtained from Avanti Polar Lipids (Alabaster, Alabama, USA). The phospholipids used in this study were 1-palmitoyl-2-oleoyl-*sn*-glycero-3-phosphocholine (POPC), 1-palmitoyl-2-oleoyl-*sn*-glycero-3-phosphate (POPA). The cell permeable forms used were 1,2-dioctanoyl-*sn*-glycero-3-phosphate (DOcPA) and 1,2-dioctanoyl-*sn*-glycerol (DOcG). Oregon Green 488-dihexadecanoylphosphatidylethanolamine (OG-PE) was obtained from Invitrogen,

Barcelona, Spain. Phorbol-12-myristate-13-acetate (PMA) and Histone III-S were purchased from Sigma Chemical Co. (Madrid, Spain).

Homology modelling

Phyre2 server was used for modeling PKC ϵ C1B (M241-V294) and PKC η C1B (N243-V297) domains. It predicts the three-dimensional (3D) structure of a protein sequence using the principles and techniques of homology modeling (20). The server selected six templates to model the proteins based on heuristic to maximize confidence (99%), percentage identity and alignment coverage. Energy minimization was done using GROMOS96 included on SwissPDBViewer 4.1.0 and this gave total energy values of -2294.564 kJ/mol (C1B ϵ) and -2052.135 kJ/mol (C1B η) (34). The program VERIFY3D was used to validate the models (35). The scores for C1B ϵ were in a range from 0 to 0.39, except D257 that was scored -0.01. The scores for C1B η were in a range from 0 to 0.26, except S264, L265, M270, R271 and Q272 that were scored slightly below 0 (from -0.01 to -0.03). The model space analysis was performed by using the Ramachandran Plot (RAMPAGE) (36). The results indicated that 86% of the residues are in the favored region and 14% in the allowed region for C1B ϵ . For C1B η , the Ramachandran Plot showed that 88% of the amino acids were in the favored, 10% in the allowed region, and only Pro290 was located in the outlier region. Multiple sequence alignment was performed with CLUSTAL O (1.2.4) (37).

For the SNARE complex, individual proteins were modelled by using SWISS-MODEL ExPasy server (38) (PDB coordinates used as templates were 6MDN (SNAP23, aa 7-208), 4WY4 (VAMP8 aa 10-64) and 1L4A (STX4, aa 211-267). The SNARE complex was modelled by 3D structural alignment to the SNARE complex formed by SNAP29/STX17/VAMP8 (PDB: 4WY4) by using PyMol. Further refinement and energy minimization of the complex was performed by using sequential runs in ClusPro (39). First step used the coordinates obtained in the structural

alignment being STX4+VAMP8 (receptor) and SNAP23 (ligand). The second run used the best model obtained in the first run for SNAP23+VAMP8 (receptor) and STX4 (ligand). To choose the best complex solutions, we took two references: i) orientation of the four helices in the complex has to be parallel Nt-Ct direction. ii) conserved ionic layer of the coiled-coil has to be formed by the side chains of residues VAMP8R36, STX4E230, SNAP23Q40 and SNAP23Q179 through hydrogen bonding. Phosphorylation states were generated with PyTMs plugin in PyMol (40).

Calculation of Electrostatic Potentials

The electrostatic potential at the surface of the C1 domain was explored with the Adaptive Poisson-Boltzmann Solver (APBS) plug-in (41) within PyMOL, using default values of the server. Individual C1B domains were submitted to the PDB2PQR server and charged at pH 7.0. PARSE atomic charges and radii were used, modified slightly to include values for zinc (+2 charge, 0.74 Å radius) and to modify the values for the eight zinc-coordinating residues, which were each given a partial charge of -0.5 to set the net charge for each zinc-binding motif to zero (42). Protein and solvent dielectric constants were set to 2 and 80, respectively. The solvent radius used was 1.4 Å and the ionic radius used was 2.0 Å. The graphical representations of the calculated electrostatic potential surfaces in 100 mM monovalent ions at $\pm 5kT/e$ were displayed using PyMOL (<http://www.pymol.org>). Docking of the 1,2-diacetyl-*sn*-glycerol (DAG) molecule was performed with SwissDock. The protein was kept fixed, and the ligand (1,2-diacetyl-*sn*-glycerol) had freely rotating bonds.

Evolutionary conservation analysis

The evolutionary conservation analysis of C1B ϵ domain was performed using the ConSurf server (26), which determined the degree of evolutionary conservation of each amino-acid. The following parameters were selected for this analysis: 3D model predicted by HHPred, homologous search algorithm: HMMER; number of iterations: 1; E-value cut-off: 0.0001; protein database: UniProt; reference sequence: closest; number of reference sequences selected: 150; maximum sequence identity: 95%; minimum identity for counterparts: 35%; alignment method: MAF; calculation method: Bayesian; and evolutionary substitution model: best fit (default).

Construction of the Expression plasmids

PKC ϵ cDNA was a gift from Drs. Nishizuka and Y. Ono (Kobe University, Kobe, Japan). N-Terminal fusion of rat PKC ϵ to green fluorescent protein (EGFP) was generated essentially as described previously (10).

The cDNA encoding the C1A domain (residues 169-220) and the C1B domain of PKC ϵ (residues 242-292) were amplified by PCR using the following primers:

C1A ϵ : 5' CCGAAGCTTGTCAATGGCCACAAG

C1A ϵ : 3' AAATCCCGGGTCATAGCCCAGCGCACTTC

C1B ϵ : 5' CCGAAGCTTAACATGCCCCACAAG

C1B ϵ : 3' GTTAACACCCACCTGACTGGGCCCTAAA

C-terminal fusions of isolated C1B domains were generated by inserting cDNAs into the multiple cloning site of the pECFP vector modified and described (9). The ECFP-C1B and PKC ϵ -EGFP mutants were generated by using the Quikchange XL site-directed mutagenesis Kit (Stratagene, La Jolla, CA, USA).

All constructs were confirmed by DNA sequencing in the Research and Development Support Center (CAID), Universidad de Murcia (Spain).

Cell culture and transfection

HEK293 cells were grown in Dulbecco's modified Eagle's medium (DMEM) with 10% fetal bovine serum (FBS). Cells were transfected with 2 µg DNA/6 cm plate using Lipofectamine-2000 (Invitrogen, Carlsbad, CA) following the instructions provided by the manufacturer. The cells were lysed 24 hours after transfection and the supernatants were used for the fluorescence experiments as described by Sanchez-Bautista et al. (9).

RBL-2H3 cells were cultured in Dulbecco's modified Eagle's medium (DMEM) supplemented with 15% (v/v) fetal bovine serum (FBS), antibiotic (penicillin 50 units/ml and streptomycin 50 µg/ml), and 4 mM glutamine. The transfection protocol and preparation of the cells for *in vivo* stimulation have been described previously by (10). To transfect RBL-2H3 cells, $10 \cdot 10^6$ harvested cells were resuspended in electroporation buffer (120 mM NaCl, 5.5 mM KCl, 2.8 mM MgCl₂, 25 mM glucose, 20 mM HEPES, pH 7.2) and 40 µg of cDNA. The cells were electroporated in a GenePulser (Bio-Rad, Hercules, CA) with one 200 V/10 ms square wave pulse and immediately placed on ice for 5 min before being plated in a flask or on glass coverslips and incubated at 37 °C for 4–6 h, after which the growth medium was renewed. To select stable transfected cells, they were incubated in their regular growth medium containing G418 (700 mg/mL) for three weeks. To stimulate cells, 4 mg/ml 1,2-Dioctanoylglycerol (DOcG) and 5 mg/ml 1,2-dioctanoyl-*sn*-phosphatidic acid (DOcPA) were added for 5 minutes. They were dissolved in dimethyl sulfoxide and diluted to the final concentration with HBS buffer (120 mM NaCl, 25 mM glucose, 5.5 mM KCl, 1.8 mM CaCl₂, 1 mM MgCl₂, 20 mM HEPES pH 7.2) shortly before the experiment.

Cell Sorting

Stable RBL-2H3 cell lines, transfected PKC ϵ -WT-GFP and PKC ϵ -MUT-GFP selected with G418 antibiotic, were sorted using a Cell Sorter SONY SH800Z with 488 nm excitation laser and detecting and sorting fluorescent single cells with 525 nm detector.

Western blotting

Cells were lysed for 20 min on ice in the following buffer: 150 mM NaCl, 50 mM Tris pH 7.4, 1% NP40, 10% glycerol, completed with protease inhibitors and phosphatase inhibitors. Cell lysates were passed 10 times through 26G^{1/2} needles, centrifuged and frozen for western-blot analysis.

The proteins of cell lysates were heat-denatured in Laemmli sample buffer and separated on 17% gels by SDS-PAGE, transferred to nitrocellulose membrane (Amersham Protran). After blocking with 2% BSA in TBST for 2 hours, membranes were incubated overnight with anti-SNAP23 antibody (10825-1-AP, Proteintech; dilution 1/500), anti-VAMP8 antibody (ab76021, abcam, dilution 1/2000), anti-GAPDH antibody (60004-1-Ig, Proteintech, dilution 1/5000), anti-STX4 antibody (CAT14988-1-AP, Proteintech, dilution 1/500). Signals were visualized with enhanced chemiluminescence detection reagent (WesternBright Quantum kit, Advantisa). Blots were analysed with ImageQuant TL 8.1 (Cytiva) image analysis software.

β -hexosaminidase assay

Secretion was assessed by measuring release of β -hexosaminidase. Cells were seeded (1×10^5 cells) in 24 wells overnight. Then, cells were washed using Tyrode's buffer (135 mM NaCl, 5 mM KCl, 1.8 mM CaCl₂, 1.0 mM MgCl₂, 5.6 mM Glucose, 20 mM HEPES, and 1 mg/ml BSA at pH 7.4). After, cells were stimulated for 1 hour at 37°C as appropriate in Tyrode's buffer. The supernatant (100 μ L) was mixed with 100 μ L p-NAG (1 mM) in 0.1 M sodium citrate buffer (pH 4.5) in a 96-well plate, and then incubated for 1 h at 37 °C. The reaction was terminated by adding stop buffer (0.2 M, glycine pH 10.7). The total β -hexosaminidase activity was also measured using a whole

cell lysate of the RBL-2H3 cells lysed with 0.1% Triton X100. Absorbance at 405 nm was measured using a FLUOstar Omega microplate reader.

Immunofluorescence assay

RBL-2H3 cells were plated in WillCo-dish Glass Bottom dish, “Series GWST-3522” (WillCo wells B.V., Amsterdam-NL) for two days, stimulated if applicable and fixed with 4 % FA in PBS for 15 min. After washing, cells were permeabilized with 0,1% Triton X-100 in PBS for 10 min and blocked with 1% bovine serum albumin (BSA) for 30 min at room temperature. Primary antibodies were incubated for 1 hour: Rabbit monoclonal [EP2629Y] against VAMP8 (ab76021, Abcam; dilution 1/100), Rabbit polyclonal against SNAP23 (ab4114, Abcam; dilution 1/200) and Rabbit polyclonal to Syntaxin 4 antibody [N2C3] (GTX114806, Genetex; dilution 1/100). Antibodies were diluted in PBS containing 1% BSA and 0.15 % Saponin. After incubation step, cells were washed three times followed by 1-hour incubation with fluorescent-labeled secondary antibody in a dark room: Goat Anti-Rabbit IgG H&L (Alexa Fluor® 647) preadsorbed (ab150083, abcam). Finally, cells were washed three times and kept in PBS to obtain images under a TIRF microscope.

Confocal Microscopy and Image analysis

In vivo cells expressing the full length PKC ϵ -EGFP, its mutant, or ECFP-C1 domain constructs, were washed with HBS and examined using a TCS SP2 confocal system (Leica, Heidelberg, Germany) with a Nikon PLAN APO-CS 63x 1.2 numerical aperture water immersion objective. Confocal images were obtained by excitation at 405 nm and emission wavelengths at 470–475 nm for ECFP, or by excitation at 488 nm and emission wavelengths at 510–530 nm for EGFP. During imaging, cells were stimulated with DNP-HSA, DOcG or DOcPA. Series of 120-240 confocal images were recorded for each experiment at time intervals of 3 s. Background was subtracted

from the images before the calculations were performed. The time series were analyzed using ImageJ NIH software FIJI (43). An individual analysis of protein translocation for each cell was performed by tracing a line intensity profile across the cell (10). The relative increase in the amount of enzyme localized in the plasma membrane for each time point was calculated by using the ratio $R = I_{mb}/(I_{cyt}+I_{mb})$, where I_{mb} is the fluorescence intensity at the plasma membrane and I_{cyt} is the average cytosolic fluorescence intensity. Mean values are given SE of the mean.

Total Internal Reflection Fluorescence (TIRF) microscopy and puncta analysis

Immunofluorescences of RBL-2H3 in PBS were imaged under a Thunder Leica DMI8 inverted microscope equipped with Total Internal Reflection Fluorescence (TIRF) (Leica, Weztlar). This microscope was used for TIRF imaging at the plasma membrane with a 488 nm laser for EGFP (emission range 500-546 nm) and 638 nm laser for AlexaFluor 647 (emission range 658-750 nm). TIRF images were captured using a DFC 9000 GTC sCMOS camera (Leica, Weztlar) with 16 bits and HC PL APO 100x/1.47 OIL CORR TIRF objective (Leica, Weztlar). Images were acquired sequentially to ensure the same penetration depth (130 nm) by automatic adjustment of the TIRF system.

PKC ϵ -EGFP microdomains formation in the plasma membrane were characterized by drawing a 15 micrometer line to analyse the average amplitude of the fluorescence intensity profile of each cell before and after stimulation (LASX Core software, Leica). The results were expressed as the average increment of fluorescence intensity and normalized by the total fluorescence scale of each micrograph (see Fig. S5B and C). SNAP23, VAMP8 and STX4, were specifically immunodetected with the corresponding primary antibodies, the secondary antibody used was conjugated to Alexa Fluor 647. Ten random micrographs were taken in each preparation to quantify the number of vesicles near the plasma membrane. Total puncta fluorescence signals were quantified using Find

Maxima plugin of FIJI software (43). Results were expressed as number of secretory vesicles per 100 μm^2 of cell area.

Statistical analysis

Statistical data analysis and visualization were performed with estimation stat database (www.estimationstats.com) (44). Using this approach, all datapoints were presented in an estimation plot to display the underlying distribution. The effect size is presented as a bootstrap 95% confidence interval (95% CI) on a separate but aligned axes, which shows the relevant effect sizes in data analysis.

Purification of Protein Kinase C ϵ and mutants

HEK293 cells were cultured in 9-cm plates and once they reached 80% confluence, they were transfected with 10 μg of cDNA of PKC ϵ -EGFP and the different mutants. Cells were harvested at 48 h posttransfection, pelleted, and resuspended in lysis buffer composed by 20 mM Tris-HCl pH 8.0, 10 mM EGTA, 2 mM EDTA, 0.25 M sucrose, 1 mM phenylmethylsulfonyl fluoride, 10 $\mu\text{g}/\text{ml}$ leupeptine, 100 μM Na_3VO_4 and 50 mM NaF with a ratio: 5 ml lysis buffer / g of cells. The pellet was disrupted by sonication on ice for 6 seconds 16 times and the resulting lysate was centrifuged at 13,000 rpm for 30 min at 4°C. The supernatant was ultra-centrifuged to 35.000xg during 30 min at 4°C and the resulting supernatant was applied to a SOURCE 15PHE 4.6/100 PE® column (GE Healthcare bio-Sciences AB; Uppsala, Sweden) previously equilibrated with Buffer E (20 mM Tris-HCl pH 8.0, 0.5 mM EGTA, 0.5 mM EDTA). The elution of the bounded protein was performed by using a saline gradient from 0 to 1 M of KCl dissolved in buffer E at a flow rate of 0.5 ml/min. Fractions were checked by western blot and the protein was concentrated by using a 30K Ultrafree centrifugal filter device (Millipore, Billerica, MA).

Kinase Activity Assay

Large unilamellar vesicles (LUVs) for activity assays were prepared as described by (45). The kinase activity was assayed *in vitro* with purified wild-type and mutant PKC ϵ by measuring the incorporation of ^{32}P i into the substrate histone III-S as was described previously (10). Briefly, the reaction was started by addition of 0.03 μg of wild-type PKC ϵ , or mutant, to a 45- μl reaction mixture containing 20 mM Tris-HCl pH 8.0, 0.2 mM EGTA, 5 mM MgCl $_2$, 0.4 mg/ml histone III-S, 50 μM ATP with [^{32}P]ATP (300,000 cpm/nmol) and 625 μM final concentration of lipids. After 20 min at 25°C, the reaction was stopped using 1 ml of ice-cold 25% (w/v) trichloroacetic acid and 1 ml of 0.05% (w/v) bovine serum albumin. The reaction mixture was then stored on ice for 30 min and the proteins were collected on a 2.5-cm-diameter glass fiber filter and washed twice with 10% trichloroacetic acid. The level of incorporation of ^{32}P i was measured by liquid scintillation counting. Background specific activity in the absence of lipids was also measured and subtracted to that obtained in the presence of the distinct phospholipid mixtures. Additional control experiments were performed with mock cell lysates to eliminate the endogenous activity, which represented less than 1% of the total enzyme activity measured. Kinase activity assays were repeated at least for three times.

Supplementary Materials

Table S1. Plasma membrane translocation of C1B ϵ -ECFP parameters in RBL-2H3 cells stimulated with DNP-HSA, DOcPA and/or DOcG.

Fig. S1. Plasma membrane localization of C1B ϵ -ECFP domain in RBL-2H3 cells.

Table S2. Binding parameters of C1B ϵ -ECFP mutant domains to phospholipid vesicles.

Table S3. Plasma membrane translocation parameters of PKC ϵ -EGFP in RBL-2H3 cells stimulated with DNP-HSA, DOcPA and/or DOcG.

Fig. S2. Plasma membrane localization of PKC ϵ -EGFP-WT in RBL-2H3 cells activated by DOcPA and DOcG.

Fig. S3. Stable RBL-2H3 cell lines expressing PKC ϵ -WT-EGFP and PKC ϵ -4MUT-EGFP.

Fig. S4. VAMP8 and STX4 do not exhibit electrophoretic mobility shifts due to phosphorylation.

Fig. S5. TIRF characterization of PKC ϵ localization at the plasma membrane when RBL-2H3 cells are stimulated with PA.

Table S4. Phosphorylation sites in the SNARE complex (SNAP23/STX4/VAMP8) determined in PhosphoSitePlus^R.

REFERENCES:

1. H. Morita, H. Saito, K. Matsumoto, S. Nakae, Regulatory roles of mast cells in immune responses. *Semin Immunopathol* **38**, 623-629 (2016).
2. S. Kraft, J. P. Kinet, New developments in FcepsilonRI regulation, function and inhibition. *Nat Rev Immunol* **7**, 365-378 (2007).
3. Z. Peng, M. A. Beaven, An essential role for phospholipase D in the activation of protein kinase C and degranulation in mast cells. *J Immunol* **174**, 5201-5208 (2005).
4. Y. Liu, Y. Su, X. Wang, Phosphatidic acid-mediated signaling. *Adv Exp Med Biol* **991**, 159-176 (2013).
5. M. A. Zhukovsky, A. Filograna, A. Luini, D. Corda, C. Valente, Phosphatidic acid in membrane rearrangements. *FEBS Lett* **593**, 2428-2451 (2019).
6. W. F. Ochoa *et al.*, Structure of the C2 domain from novel protein kinase Cepsilon. A membrane binding model for Ca(2+)-independent C2 domains. *J Mol Biol* **311**, 837-849 (2001).
7. J. García-García, J. C. Gómez-Fernández, S. Corbalán-García, Structural characterization of the C2 domain of novel protein kinase Cepsilon. *Eur J Biochem* **268**, 1107-1117 (2001).
8. S. Corbalán-García, S. Sánchez-Carrillo, J. García-García, J. C. Gómez-Fernández, Characterization of the membrane binding mode of the C2 domain of PKC epsilon. *Biochemistry* **42**, 11661-11668 (2003).
9. S. Sanchez-Bautista, S. Corbalan-Garcia, A. Perez-Lara, J. C. Gomez-Fernandez, A Comparison of the Membrane Binding Properties of C1B Domains of PKC gamma, PKC delta, and PKC epsilon. *Biophysical Journal* **96**, 3638-3647 (2009).
10. M. Jose Lopez-Andreo, J. C. Gomez-Fernandez, S. Corbalan-Garcia, The simultaneous production of phosphatidic acid and diacylglycerol is essential for the translocation of protein kinase Cepsilon to the plasma membrane in RBL-2H3 cells. *Mol Biol Cell* **14**, 4885-4895 (2003).
11. A. L. Egea-Jiménez, S. Corbalán-García, J. C. Gómez-Fernández, The C1B domains of novel PKC ϵ and PKC η have a higher membrane binding affinity than those of the also novel PKC δ and PKC θ . *Biochim Biophys Acta* **1838**, 1898-1909 (2014).
12. J. R. Woska, M. E. Gillespie, Small-interfering RNA-mediated identification and regulation of the ternary SNARE complex mediating RBL-2H3 mast cell degranulation. *Scand J Immunol* **73**, 8-17 (2011).
13. R. Hepp *et al.*, Phosphorylation of SNAP-23 regulates exocytosis from mast cells. *J Biol Chem* **280**, 6610-6620 (2005).
14. S. Malmersjö *et al.*, Phosphorylation of residues inside the SNARE complex suppresses secretory vesicle fusion. *EMBO J* **35**, 1810-1821 (2016).

15. E. Y. Chang *et al.*, Functional effects of overexpression of protein kinase C-alpha, -beta, -delta, -epsilon, and -eta in the mast cell line RBL-2H3. *J Immunol* **159**, 2624-2632 (1997).
16. H. Nechushtan, M. Leitges, C. Cohen, G. Kay, E. Razin, Inhibition of degranulation and interleukin-6 production in mast cells derived from mice deficient in protein kinase Cbeta. *Blood* **95**, 1752-1757 (2000).
17. G. Li, J. J. Lucas, E. W. Gelfand, Protein kinase C alpha, betaI, and betaII isozymes regulate cytokine production in mast cells through MEKK2/ERK5-dependent and -independent pathways. *Cell Immunol* **238**, 10-18 (2005).
18. E. Razin, Z. Szallasi, M. G. Kazanietz, P. M. Blumberg, J. Rivera, Protein kinases C-beta and C-epsilon link the mast cell high-affinity receptor for IgE to the expression of c-fos and c-jun. *Proc Natl Acad Sci U S A* **91**, 7722-7726 (1994).
19. K. S. Bell *et al.*, The role of individual protein kinase C isoforms in mouse mast cell function and their targeting by the immunomodulatory parasitic worm product, ES-62. *Immunol Lett* **168**, 31-40 (2015).
20. L. A. Kelley, S. Mezulis, C. M. Yates, M. N. Wass, M. J. Sternberg, The PyMOL web portal for protein modeling, prediction and analysis. *Nat Protoc* **10**, 845-858 (2015).
21. A. Grosdidier, V. Zoete, O. Michielin, SwissDock, a protein-small molecule docking web service based on EADock DSS. *Nucleic Acids Res* **39**, W270-277 (2011).
22. U. Hommel, M. Zurini, M. Luyten, Solution structure of a cysteine rich domain of rat protein kinase C. *Nat Struct Biol* **1**, 383-387 (1994).
23. G. Zhang, M. G. Kazanietz, P. M. Blumberg, J. H. Hurley, Crystal structure of the cys2 activator-binding domain of protein kinase C delta in complex with phorbol ester. *Cell* **81**, 917-924 (1995).
24. R. V. Stahelin *et al.*, Diacylglycerol-induced membrane targeting and activation of protein kinase Cepsilon: mechanistic differences between protein kinases Cdelta and Cepsilon. *J Biol Chem* **280**, 19784-19793 (2005).
25. M. A. Lomize, I. D. Pogozheva, H. Joo, H. I. Mosberg, A. L. Lomize, OPM database and PPM web server: resources for positioning of proteins in membranes. *Nucleic Acids Res* **40**, D370-376 (2012).
26. H. Ashkenazy *et al.*, ConSurf 2016: an improved methodology to estimate and visualize evolutionary conservation in macromolecules. *Nucleic Acids Res* **44**, W344-350 (2016).
27. K. Suzuki, I. M. Verma, Phosphorylation of SNAP-23 by IkkappaB kinase 2 regulates mast cell degranulation. *Cell* **134**, 485-495 (2008).
28. M. Midorikawa, Real-time imaging of synaptic vesicle exocytosis by total internal reflection fluorescence (TIRF) microscopy. *Neurosci Res* **136**, 1-5 (2018).
29. P. Naskar, N. Puri, Phosphorylation of SNAP-23 regulates its dynamic membrane association during mast cell exocytosis. *Biol Open* **6**, 1257-1269 (2017).
30. S. Corbalán-García, J. C. Gómez-Fernández, Protein kinase C regulatory domains: the art of decoding many different signals in membranes. *Biochim Biophys Acta* **1761**, 633-654 (2006).
31. L. Li, I. Vorobyov, T. W. Allen, The different interactions of lysine and arginine side chains with lipid membranes. *J Phys Chem B* **117**, 11906-11920 (2013).
32. Q. J. Wang *et al.*, Role of hydrophobic residues in the C1b domain of protein kinase C delta on ligand and phospholipid interactions. *J Biol Chem* **276**, 19580-19587 (2001).
33. P. V. Hornbeck *et al.*, 15 years of PhosphoSitePlus®: integrating post-translationally modified sites, disease variants and isoforms. *Nucleic Acids Res* **47**, D433-D441 (2019).
34. W. F. van Gunsteren *et al.*, *Biomolecular Simulation: The GROMOS96 Manual and User Guide*. (vdf Hochschulverlag AG an der ETH Zürich and BIOMOS b.v.: Zürich, Groningen., 1996), pp. 1-1042.
35. D. Eisenberg, R. Lüthy, J. U. Bowie, VERIFY3D: assessment of protein models with three-dimensional profiles. *Methods Enzymol* **277**, 396-404 (1997).
36. S. C. Lovell *et al.*, Structure validation by Calpha geometry: phi,psi and Cbeta deviation. *Proteins* **50**, 437-450 (2003).
37. H. McWilliam *et al.*, Analysis Tool Web Services from the EMBL-EBI. *Nucleic Acids Res* **41**, W597-600 (2013).
38. A. Waterhouse *et al.*, SWISS-MODEL: homology modelling of protein structures and complexes. *Nucleic Acids Res* **46**, W296-W303 (2018).
39. D. Kozakov *et al.*, The ClusPro web server for protein-protein docking. *Nat Protoc* **12**, 255-278 (2017).
40. A. Warnecke, T. Sandalova, A. Achour, R. A. Harris, PyTMs: a useful PyMOL plugin for modeling common post-translational modifications. *BMC Bioinformatics* **15**, 370 (2014).
41. S. Unni *et al.*, Web servers and services for electrostatics calculations with APBS and PDB2PQR. *J Comput Chem* **32**, 1488-1491 (2011).

42. Y. Pu *et al.*, Effects on ligand interaction and membrane translocation of the positively charged arginine residues situated along the C1 domain binding cleft in the atypical protein kinase C isoforms. *J Biol Chem* **281**, 33773-33788 (2006).
43. J. Schindelin *et al.*, Fiji: an open-source platform for biological-image analysis. *Nat Methods* **9**, 676-682 (2012).
44. H. J. T. T, A. S, C. H, C.-C. A, Moving Beyond P Values: Data Analysis With Estimation Graphics. *Nature methods* **16**, (2019).
45. A. L. Egea-Jiménez, A. Pérez-Lara, S. Corbalán-García, J. C. Gómez-Fernández, Phosphatidylinositol 4,5-bisphosphate decreases the concentration of Ca²⁺, phosphatidylserine and diacylglycerol required for protein kinase C α to reach maximum activity. *PLoS One* **8**, e69041 (2013).

Acknowledgments:

Funding: Work in Murcia was supported by grants BFU2017-87222-P (MICINN, Spain-FEDER) and Fundación Séneca Region de Murcia 20885/PI/18 to S.C-G. A.L.E-J has been financed from the European Union's Horizon 2020 research and innovation program under the Marie Skłodowska-Curie grant agreement No 747025.

Author contributions: D.L-M., E.S-L and A.L.E-J performed cloning, biochemical and cell biology experiments, analysed, interpreted data, and prepared figures. J.C.G-F. and A.L.E-J designed part of the study and experiments, interpreted data, and contributed to wrote part of the manuscript; S.C-G. designed the study and experiments, performed the structural analysis, analysed, interpreted the data, prepared figures, and wrote the manuscript.

Competing interests: there are not conflict of interests.

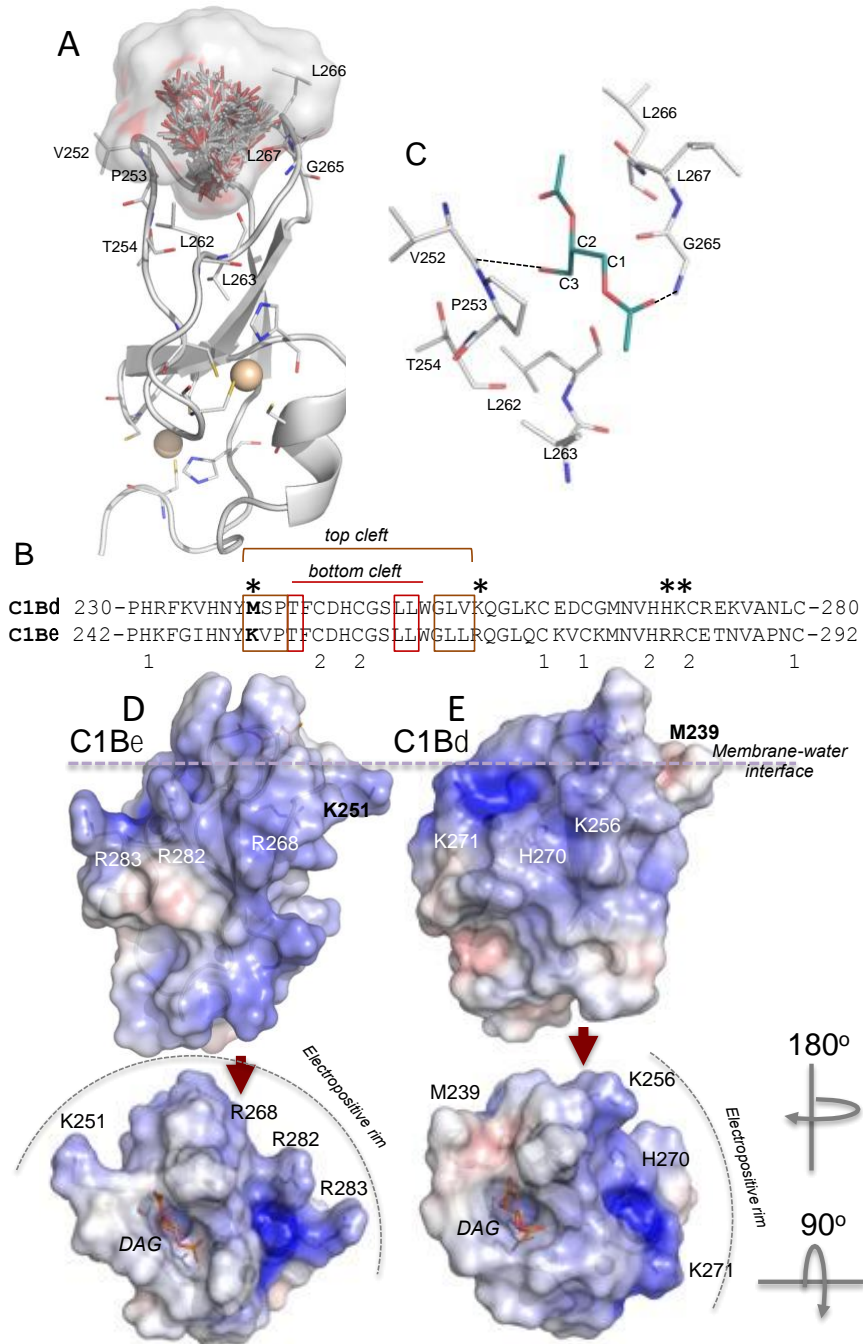


Fig. 1. The C1B domains of PKCe and PKCd exhibit different electrostatic potential. (A) Overall structure of the C1Be domain modeled by using Phyre2 (grey cartoon), side chains of the amino acid at the hydrophobic cleft are represented by sticks, the two Zn²⁺ ions (yellow sphere) and their binding sites are shown at the bottom of the domain. Top-ranked docking poses of 1,2-diacetyl-*sn*-glycerol into the C1Be domain are represented by sticks together with the average surface. (B) Primary sequence alignment of the C1Bd and C1Be domains, the key residues of the hydrophobic cleft are included in the red and yellow boxes. H and C residues involved in the Zn²⁺ binding sites are labeled with 1 and 2. Asterisks are on top of the potential residues interacting with acidic phospholipids. (C) Close up view to show the side chains of the hydrophobic binding cleft (grey), the top-ranked pose for 1,2-diacetyl-*sn*-glycerol (green stick) and the potential hydrogen bonds (dotted black lines). Charge distribution maps of C1Be (D) and C1Bd (E) with the surface colored by electrostatic potential in 100 mM monovalent ions from -5 kT/e (red) to +5 kT/e (blue). Top views of the domains exhibit the membrane interaction face with the diacylglycerol molecule represented as sticks (orange). The amplitude of the electropositive rim is indicated by the dotted lines. PDB C1Bd (1PTR).

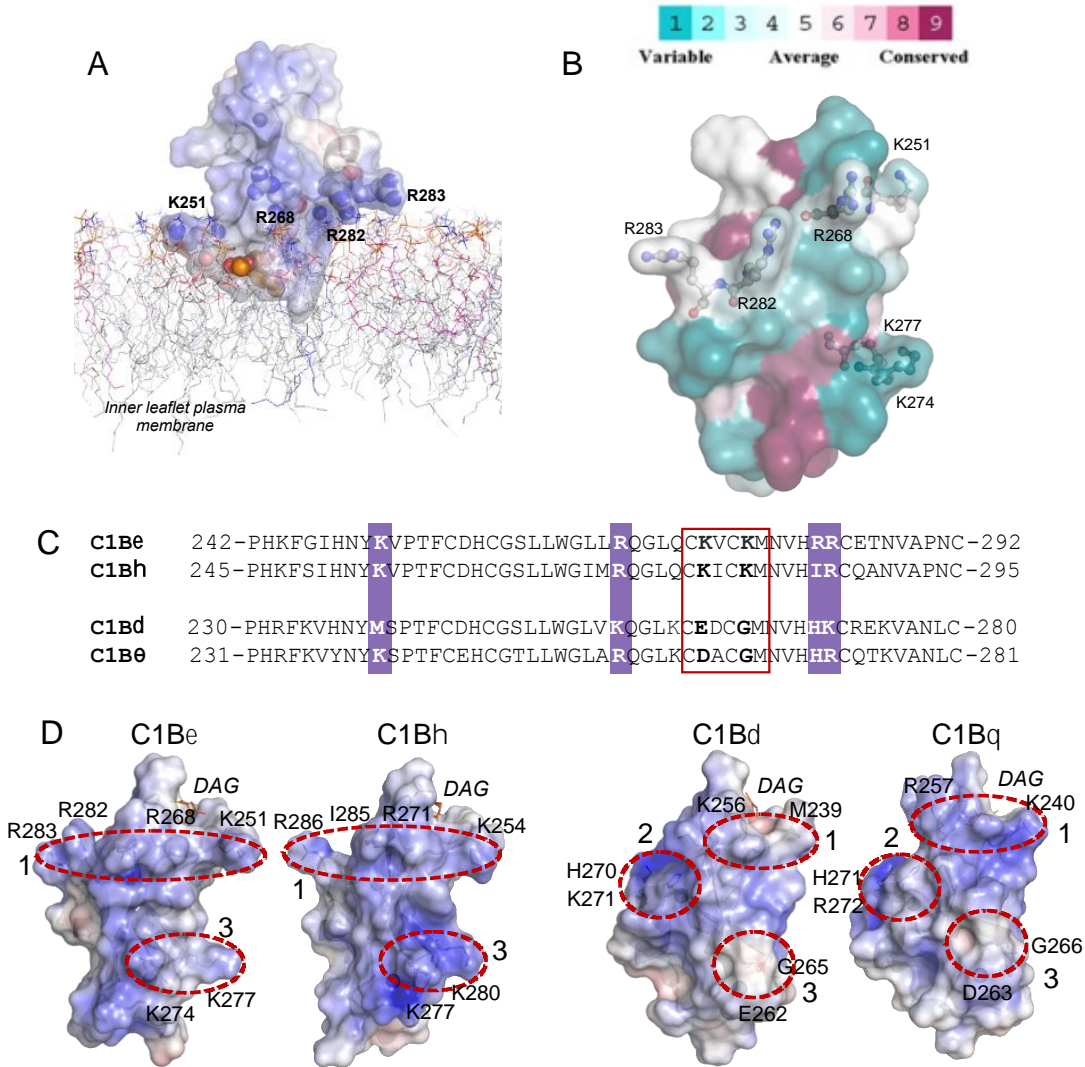


Fig. 2. 3D structural prediction finds in the C1B domain of PKCε key residues for plasma membrane localization in RBL-2H3 cells. (A) Lateral view of the electrostatic surface potential of the C1Be domain. The electrostatic potential was calculated with APBS and is projected onto the molecular surface of the domain. 3D structure prediction was modelled by using Phyre2. The 1,2-diacetyl-*sn*-glycerol molecule is shown in sphere model and was docked by using SwissDock. Side chains of R and K residues potentially involved in PA binding are shown as sphere model. OPM database was used to predict the orientation of the domain in the lipid bilayer. Membrane bilayer model (POPC/POPA 80:20) was generated with membrane builder server in CHARMM-GUI. (B) Evolutionary conservation analysis of the C1Be domain. Each amino acid is represented as surface model and colored according to its conservation score. The ConSurf coloring scheme is shown in the color-coding bar. The normalized scores calculated were 0.612 (K251), 0.203 (R268), 0.430 (R282) which are considered variable and -0.028 (R283) which is considered average conserved. Maximum value of conserved residues (-1.354), maximum value of variable residues (2.181). The K and R residues forming the basic rim are shown as ball and sticks. (C) Primary sequence alignment of the C1Be, C1Bh, C1Bd and C1Bq domains, the key residues of the basic rim are included in the purple boxes. The red box indicates the amino acidic residues (bold) that are not conserved between the two subfamilies that were classified based on their higher affinity to interact with PA. (D) Charge distribution maps of C1Be, C1Bh, C1Bd (PDB: 1PTR) and C1Bq (PDB: 4FKD) domains with the surface colored by electrostatic potential in 100 mM monovalent ions from -5 kT/e (red) to +5 kT/e (blue). Red dotted circles on the upper part of the domains are indicating the position of the side chains of amino acids forming the basic rim. Note how e and h exhibit a wide basic rim with a 3D distribution compatible with PA interaction at the plasma membrane surface (1) that is accompanied by another electropositive set of amino acids (3). However, d and q do not exhibit the basic rim and have two compartmentalized sets of amino acids (1, 2) instead, and the third one has electronegative potential (3).

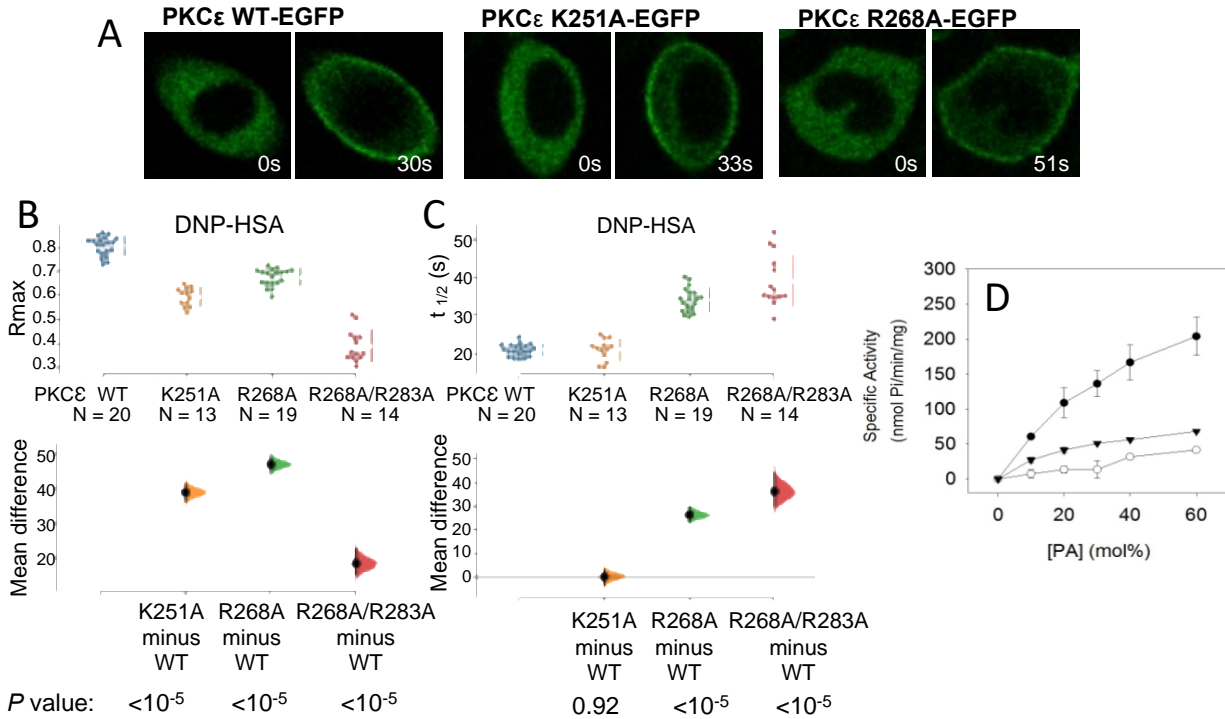


Fig. 3. The R/K residues at the basic rim in the C1B domain are essential for the PA-dependent membrane translocation of PKC ϵ in RBL-2H3 cells. (A) Confocal fluorescence images of cells expressing PKC ϵ -WT-EGFP and two of the basic rim mutants at different points of the time-lapse experiment after addition of antigen (2 μ g/ml DNP-HSA). Statistical analysis of the Rmax (B) and half-time of translocation ($t_{1/2}$) (C) parameters measured when the cells were stimulated with 2 μ g/ml DNP-HSA. Cumming estimation plots were represented by using Estimation Statistic (43). They show the raw data on the upper axes (means are shown as a gap in the right vertical line). Lower axes show the mean difference for 3 comparisons against the shared control PKC ϵ -WT-EGFP. Mean differences are plotted as bootstrap sampling distributions (5000). Each mean difference is depicted as a dot. Each 95% confidence interval is indicated by the ends of the vertical error bars. Additional permutation test was also applied to confirm these results, the P values to accept/reject the null hypothesis of no differences between the WT and the mutant proteins, are indicated below each comparison (CI 95%). (D) Specific activity of full-length PKC ϵ and basic rim mutant (PKC ϵ -EGFPK251A/R268A/R282A/R283A: PKC ϵ -4MUT-EGFP) by using large unilamellar vesicles containing POPC/POPA (99-X:X, with X being the molar fraction of POPA in each case) for PKC ϵ -WT (o) and POPC/DOG/POPA (95-X:5:X, with X being the molar fraction of POPA in each case) for PKC ϵ -WT-EGFP (\square) or PKC ϵ -4MUT-EGFP(\square). The total lipid concentration was 0.2 mM and Histone III-S was used as a substrate. Error bars indicate the SEM for triplicate determinations.

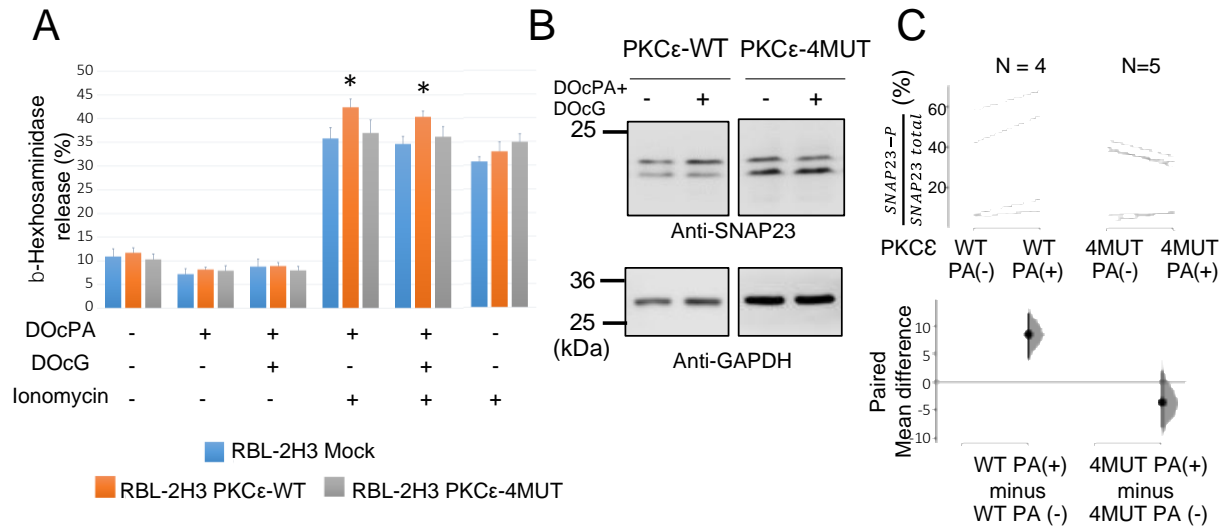


Fig. 4. PA-dependent stimulation of PKC ϵ induces phosphorylation of SNAP23 protein. (A) b-hexosaminidase release in cells induced by different types of stimulation as indicated in the figure. After DOcPA (5 μ g/ml) + Ionomycin (3 μ M) stimulation, the *P* value of the two-sided permutation t-test is 0.0418 when comparing mock and PKC ϵ -WT-EGFP cells. The *P* value of the two-sided permutation t-test is 0.706 when comparing mock and PKC ϵ -4MUT-EGFP cells. After DOcPA (5 μ g/ml) + DOcG (4 μ g/ml) + Ionomycin (3 μ M) stimulation, the *P* value of the two-sided permutation t-test is 0.0168 when comparing mock and PKC ϵ -WT-EGFP cells. The *P* value of the two-sided permutation t-test is 0.565 when comparing mock and PKC ϵ -4MUT-EGFP cells. (B) Western blot against SNAP23 of RBL-2H3 transfected cells with PKC ϵ -WT-EGFP and PKC ϵ -4MUT-EGFP stimulated with DOcPA+DOcG. SNAP23 phosphorylation was measured by the electrophoretic mobility shift detected by a 15% SDS-PAGE and western blot with anti-SNAP23 antibody on the upper image. GAPDH was used as a housekeeping protein to measure the total amount of protein loaded in the gel. (C) The ratio of phosphorylated SNAP23/total SNAP23 was measured in the two cell lines stated above in the absence and presence of DOcPA+DOcG. The raw data are plotted on the upper axes; each paired set of observations is connected by a line. The paired mean difference for 2 comparisons are shown in the Cumming estimation plot below. At least two replicates of two biologically independent experiments were performed. On the lower axes, each paired mean difference is plotted as a bootstrap sampling distribution. Mean differences are depicted as dots; 95% confidence intervals are indicated by the ends of the vertical error bars.

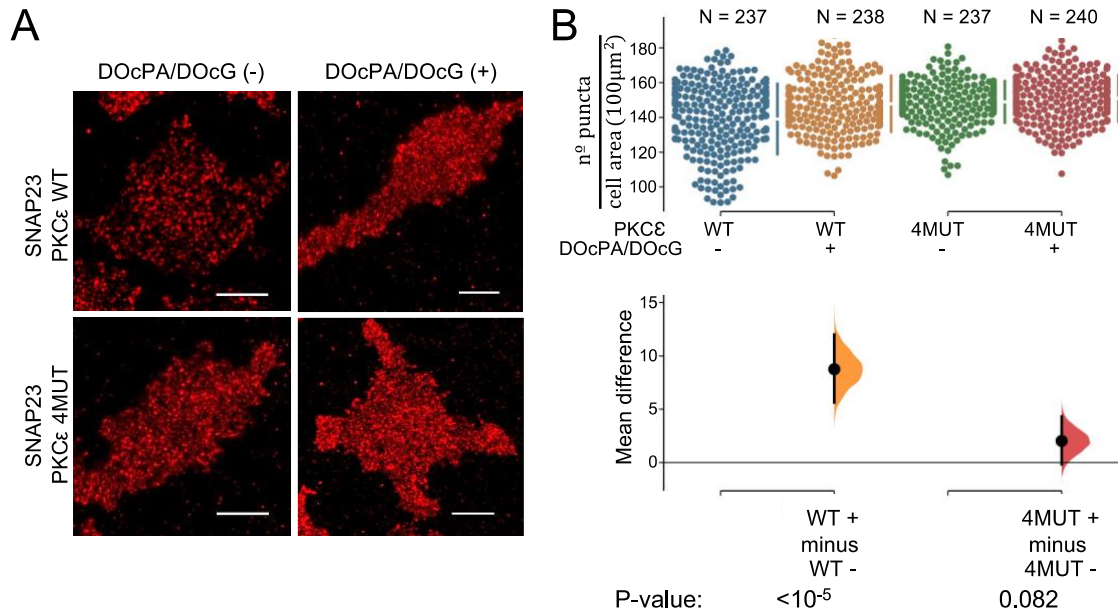


Fig. 5. PA-dependent stimulation of PKC ϵ induces an increase in the number of SNAP23-containing vesicles in RBL-2H3 cells. (A) Representative TIRF micrographs of RBL-2H3 transfected cells with PKC ϵ -WT-EGFP and PKC ϵ -4MUT-EGFP unstimulated or stimulated with DOcPA+DOcG and immunostained for endogenous SNAP23 (red). Scale bar, 10 μm . (B) Comparison of the number of puncta/cell area ($100 \mu\text{m}^2$) measured in PKC ϵ -WT-EGFP and PKC ϵ -4MUT-EGFP expressing cells. The mean difference for 2 comparisons against the unstimulated controls PKC ϵ -WT-EGFP (-) and PKC ϵ -4MUT-EGFP (-) are shown in the Cumming estimation plots. The raw data are plotted on the upper axes. On the lower axes, mean differences are plotted as bootstrap sampling distributions (5000). Each mean difference is depicted as a dot. Each 95% confidence interval is indicated by the ends of the vertical error bars. Additional permutation test was also applied to confirm these results, the P values to accept/reject the null hypothesis of no differences between resting conditions without DOcPA/DOcG (-) and after adding DOcPA+DOcG (+), are indicated below each comparison (CI 95%).

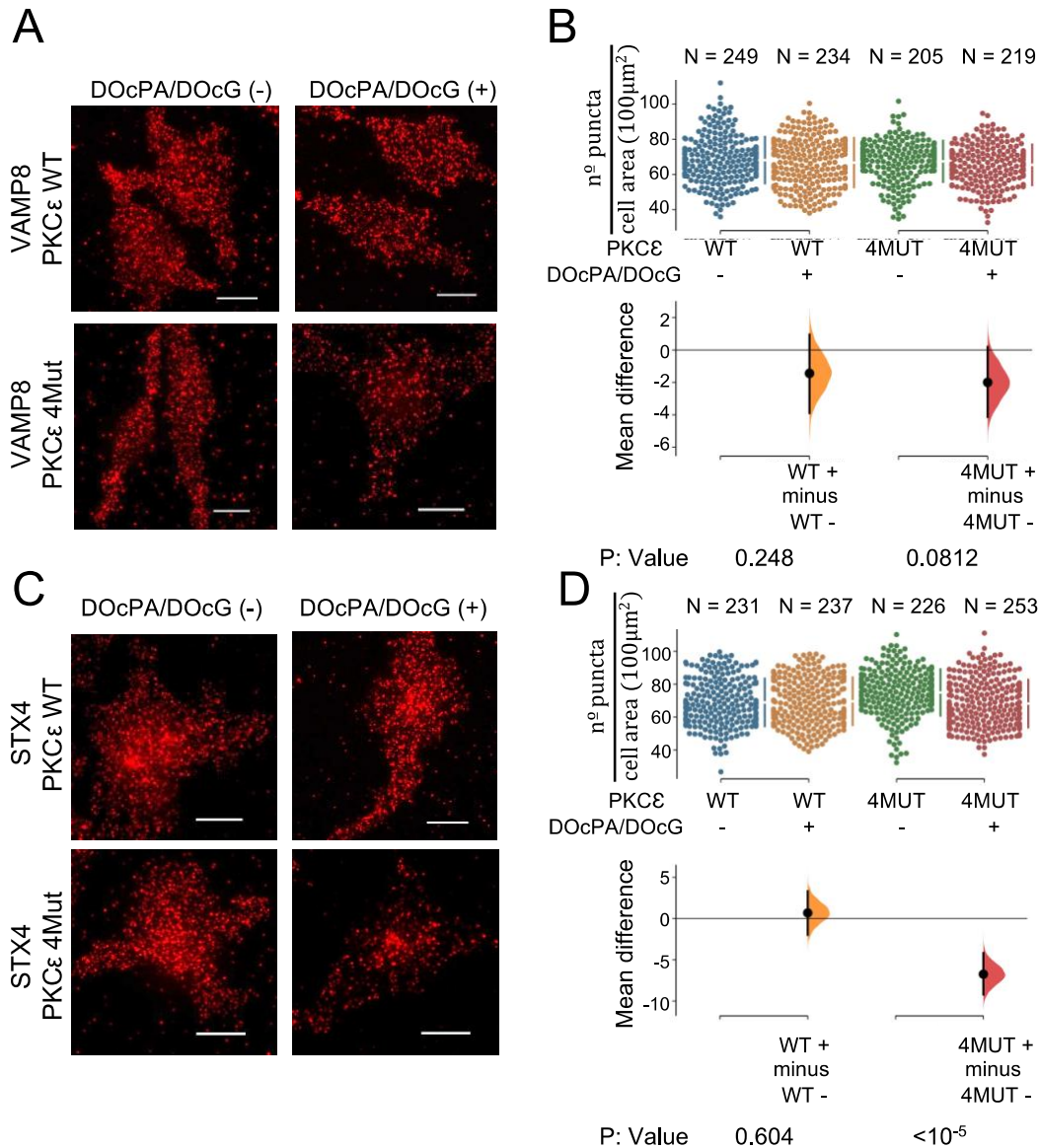


Fig. 6. PA-dependent activation of PKCε does not affect the number of VAMP8 and STX4-containing vesicles in RBL-2H3 cells. Representative TIRF micrographs of RBL-2H3 transfected cells with PKCε-WT-EGFP and PKCε-4MUT-EGFP unstimulated or stimulated with DOcPA+DOcG and immunostained for endogenous VAMP8 (red) (A) and endogenous STX4 (C). Scale bar, 10 μm. Quantification of the number of puncta/area cell (100 μm²) from three independent experiments detected from immunostaining for VAMP8 (B) and STX4 (D). (B and D) The mean difference for 2 comparisons against the unstimulated controls PKCε-WT-EGFP (-) and PKCε-4MUT-EGFP (-) are shown in the Cumming estimation plots. The raw data in (B) and (D) are plotted on the upper axes. On the lower axes, mean differences are plotted as bootstrap sampling distributions (5000). Each mean difference is depicted as a dot. Each 95% confidence interval is indicated by the ends of the vertical error bars. Additional permutation test was also applied to confirm these results, the P values to accept/reject the null hypothesis of no differences between resting conditions without DOcPA/DOcG (-) and after adding DOcPA/DOcG (+), are indicated below each comparison (CI 95%).

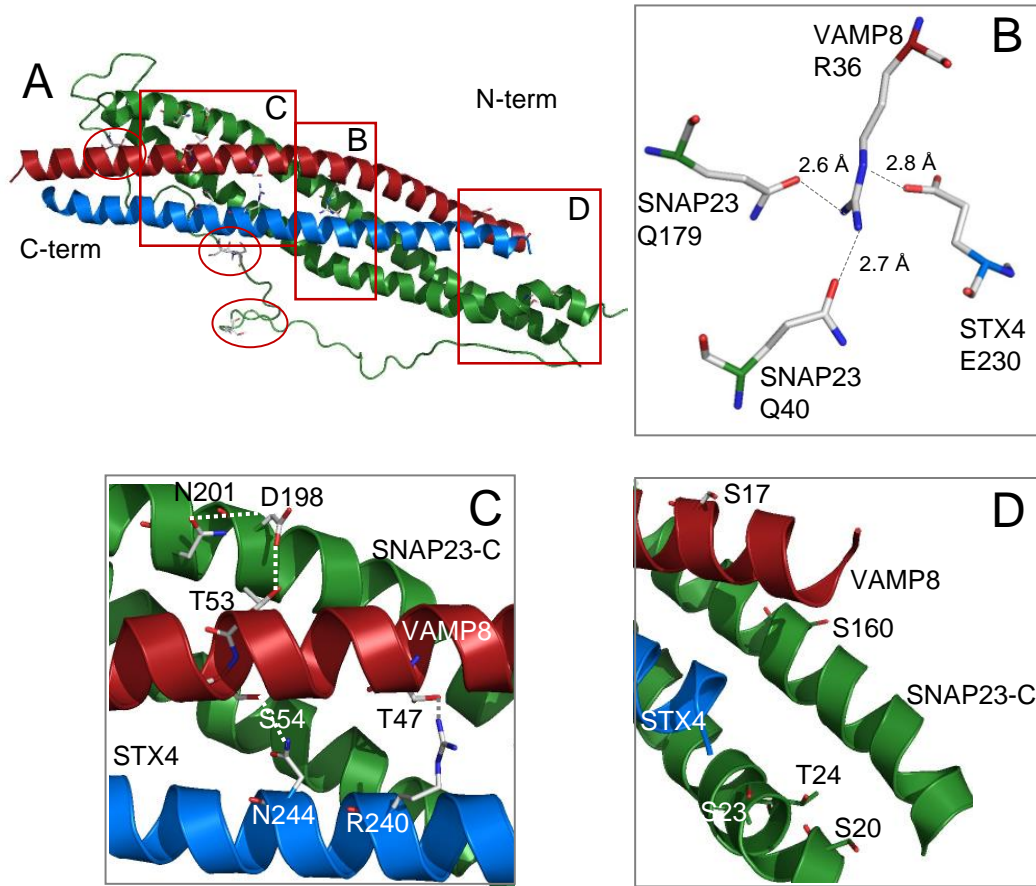


Fig.7. Modelling of the SNARE complex responsible for degranulation in RBL-2H3 cells. (A) Cartoon view of the coiled-coil formed by VAMP8 (aa 10-64) (red), STX4 (aa 211-267) (blue) and SNAP23 (aa 7-208) (green). Individual proteins were modelled by using SWISS-MODEL ExPASy server (PDB coordinates used as templates were 6mdn (SNAP23), 4wy4 (VAMP8) and 114a (STX4)). The SNARE complex was modelled by 3D structural alignment to the SNARE complex formed by SNAP29/STX17/VAMP8 (PDB: 4wy4), refinement and energy minimization of the complex was performed by using sequential runs in ClusPro. Red circles indicate the side chains of the most frequent phosphorylated residues in SNAP23. (B) Close up view of the amino acids side chains involved in the conserved ionic layer (0) consisting of VAMP8R36, STX4E230, SNAP23Q40 and SNAP23Q179. Side chains are represented as sticks, oxygen atoms in red and nitrogen atoms in blue. Hydrogen bonds are indicated by a grey dotted line with the distance in Å. (C) Close up view of the cartoon representation of the C-term region of the SNARE complex to show how the side chains of the residues frequently phosphorylated are involved in hydrogen bonding at the inside face of the coiled-coil. T47 forms a hydrogen bond with N240(STX4), S54 a hydrogen bond with N244(STX4) and T53 a hydrogen bond with D198(SNAP23) that, at the same time, is stabilized by another interaction with N201(SNAP23). (D) Close up view of the cartoon representation of the N-term region of the SNARE complex to show side chains of the residues frequently involved in phosphorylation located at the outside face of the coiled-coil.

SUPPLEMENTARY MATERIALS

Table S1. Plasma membrane translocation of C1B ϵ -ECFP parameters in RBL-2H3 cells stimulated with DNP-HSA, DOcPA and/or DOcG.

Stimulation	N cells	M.L. (%)	R_{max}	t_{1/2} (s)
<i>C1Bϵ-ECFP</i>				
2 μ g/ml DNP-HSA ^a	13	80	0.58 \pm 0.02	22 \pm 2.8
10 μ g/ml DOcPA + 4 μ g/ml DOcG	16	94	0.50 \pm 0.01	2.7 \pm 0.4
<i>C1Bϵ-ECFP/K251A</i>				
2 μ g/ml DNP-HSA	24	58	0.55 \pm 0.03	24 \pm 3
20 μ g/ml DOcPA	26	0	---	---
8 μ g/ml DOcG	19	73	0.34 \pm 0.01	8 \pm 1
4 μ g/ml DOcG	21	0	---	---
20 μ g/ml DOcPA + 4 μ g/ml DOcG	18	76	0.40 \pm 0.03	7 \pm 1
<i>C1Bϵ-ECFP/R268A</i>				
2 μ g/ml DNP-HSA	16	50	0.47 \pm 0.02	28 \pm 4
20 μ g/ml DOcPA	22	18	0.12 \pm 0.01	17 \pm 4
8 μ g/ml DOcG	17	35	0.35 \pm 0.02	7 \pm 1
4 μ g/ml DOcG	23	0	---	---
20 μ g/ml DOcPA + 4 μ g/ml DOcG	13	64	0.35 \pm 0.03	7 \pm 1
<i>C1Bϵ-ECFP/R282A</i>				
2 μ g/ml DNP-HSA	21	58	0.50 \pm 0.03	25 \pm 3
20 μ g/ml DOcPA	13	16	0.14 \pm 0.01	6 \pm 1
8 μ g/ml DOcG	26	35	0.27 \pm 0.05	8 \pm 2
4 μ g/ml DOcG	28	0	---	---
20 μ g/ml DOcPA + 8 μ g/ml DOcG	20	60	0.39 \pm 0.04	6 \pm 2
20 μ g/ml DOcPA + 4 μ g/ml DOcG	21	19	0.21 \pm 0.03	9 \pm 1
<i>C1Bϵ-ECFP/R283A</i>				
2 μ g/ml DNP-HSA	36	47	0.39 \pm 0.01	34 \pm 2
20 μ g/ml DOcPA	21	0	---	---
8 μ g/ml DOcG	15	79	0.36 \pm 0.02	6 \pm 1
4 μ g/ml DOcG	28	0	---	---
20 μ g/ml DOcPA + 8 μ g/ml DOcG	13	82	0.46 \pm 0.02	6 \pm 1
20 μ g/ml DOcPA + 4 μ g/ml DOcG	29	0	---	---
<i>C1Bϵ-ECFP/K251A/R268A</i>				
2 μ g/ml DNP-HSA	19	0	---	---
20 μ g/ml DOcPA	24	0	---	---
8 μ g/ml DOcG	25	12	0.15 \pm 0.01	7 \pm 1
20 μ g/ml DOcPA + 8 μ g/ml DOcG	28	0	---	---
<i>C1Bϵ-ECFP/R282A/R283A</i>				
2 μ g/ml DNP-HSA	38	0	---	---
20 μ g/ml DOcPA	26	0	---	---
8 μ g/ml DOcG	22	0	---	---
20 μ g/ml DOcPA + 8 μ g/ml DOcG	20	0	---	---
<i>C1Bϵ-ECFP/R268A/R282A/R283A</i>				
2 μ g/ml DNP-HSA	20	0	---	---
20 μ g/ml DOcPA	18	0	---	---
8 μ g/ml DOcG	18	0	---	---
20 μ g/ml DOcPA + 8 μ g/ml DOcG	15	0	---	---
<i>Converting C1Bϵ into C1Bδ-like</i>				
<i>ECFP-C1BϵK251M/R282H</i>				
2 μ g/ml DNP-HSA	28	32	0.31 \pm 0.02	37 \pm 1
20 μ g/ml DOcPA	26	0	---	---
8 μ g/ml DOcG	34	18	0.17 \pm 0.02	6 \pm 2
20 μ g/ml DOcPA + 8 μ g/ml DOcG	28	35	0.13 \pm 0.01	5 \pm 1
<i>ECFP-C1BϵR282H</i>				
2 μ g/ml DNP-HSA	26	69	0.51 \pm 0.02	25 \pm 6
20 μ g/ml DOcPA	29	31	0.19 \pm 0.03	7 \pm 2
8 μ g/ml DOcG	27	44	0.34 \pm 0.02	6 \pm 1
4 μ g/ml DOcG	20	0	---	---
20 μ g/ml DOcPA + 8 μ g/ml DOcG	24	83	0.46 \pm 0.01	5 \pm 1

^aRBL-2H3 cells were primed with 0.5 $\mu\text{g/ml}$ anti-IgE antibody for 16 h and then stimulated with 2 $\mu\text{g/ml}$ DNP-HSA. *M.L.* stands for membrane localization and indicates the percentage of cells responding to each type of stimulation with plasma membrane translocation. R_{max} is the maximal relative increase in plasma membrane localization of the protein. $t_{1/2}$ is the half-time of maximal translocation.

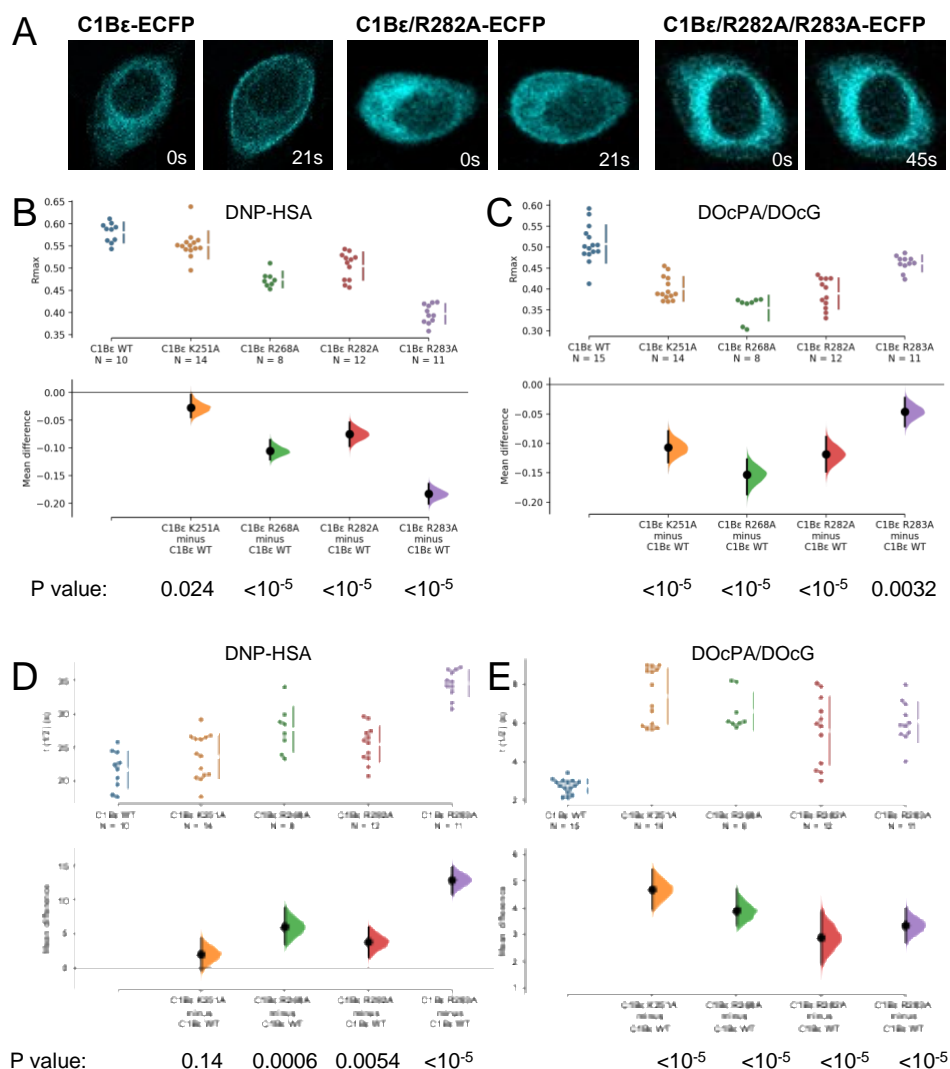


Fig. S1. Plasma membrane localization of C1B ϵ -ECFP domain in RBL-2H3 cells. (A) Confocal fluorescence images of cells expressing C1B ϵ -WT-ECFP and three of the basic rim mutants at different points of the time lapse experiment after addition of antigen (2 $\mu\text{g/ml}$ DNP-HSA). (B) Statistical analysis of the R_{max} parameter measured when the cells were stimulated with 2 $\mu\text{g/ml}$ DNP-HSA (C) or 10 $\mu\text{g/ml}$ DOcPA + 4 $\mu\text{g/ml}$ DOcG (C1B ϵ -WT-ECFP) and 20 $\mu\text{g/ml}$ DOcPA + 4 $\mu\text{g/ml}$ DOcG (C1B ϵ -ECFP mutants). (D) Statistical analysis of the half-time of translocation ($t_{1/2}$) measured when the cells were stimulated with 2 $\mu\text{g/ml}$ DNP-HSA (E) or 10 $\mu\text{g/ml}$ DOcPA + 4 $\mu\text{g/ml}$ DOcG (C1B ϵ -WT-ECFP) and 20 $\mu\text{g/ml}$ DOcPA + 4 $\mu\text{g/ml}$ DOcG (C1B ϵ -ECFP mutants). The mean difference for 4 comparisons against the shared control C1B ϵ -WT-ECFP are shown in the Cumming estimation plots. The raw data are plotted on the upper axes (means are shown as a gap in the right vertical line). On the lower axes, mean differences are plotted as bootstrap sampling distributions (5000). Each mean difference is depicted as a dot and each 95% confidence interval is indicated by the ends of the vertical error bars. Additional permutation test was also applied to confirm these results, the P values to accept/reject the null hypothesis of no differences between the WT and the mutant proteins, are indicated below each comparison (CI 95%).

Table S2. Binding parameters of C1B ϵ -ECFP mutant domains to phospholipid vesicles^a.

	POPC/POPA/OGPE (75:20:5)		POPC/POPA/DOG/OGPE (70:20:5:5)	
	ΔF_{\max} (%)	K_D (μ M)	ΔF_{\max} (%)	K_D (μ M)
Wild-type C1B ϵ -ECFP	0.58 \pm 0.04	3.03 \pm 0.35	0.67 \pm 0.02	1.18 \pm 0.06
C1B ϵ K251A-ECFP	0.52 \pm 0.04	7.98 \pm 0.77	0.57 \pm 0.03	2.05 \pm 0.15
C1B ϵ R268A-ECFP	0.39 \pm 0.01	13.17 \pm 0.11	0.54 \pm 0.02	7.34 \pm 0.92
C1B ϵ R282A-ECFP	0.53 \pm 0.04	11.57 \pm 0.69	0.54 \pm 0.02	2.32 \pm 0.09
C1B ϵ R283A-ECFP	0.40 \pm 0.01	15.43 \pm 0.95	0.43 \pm 0.02	2.14 \pm 0.76
C1B ϵ K251A/R268A-ECFP	0.33 \pm 0.01	45.12 \pm 1.01	0.55 \pm 0.02	16.29 \pm 0.43
C1B ϵ R268A/R283A-ECFP	0.27 \pm 0.04	45.59 \pm 0.69	0.68 \pm 0.01	10.57 \pm 0.91
C1B ϵ R282A/R283A-ECFP	0.31 \pm 0.03	45.12 \pm 0.19	0.63 \pm 0.02	10.10 \pm 0.54
C1B ϵ K251A/R268A/R282A-ECFP	0.19 \pm 0.02	57.10 \pm 0.68	0.31 \pm 0.01	56.36 \pm 0.48
C1B ϵ K251A/R282A/R283A-ECFP	0.19 \pm 0.01	53.21 \pm 0.69	0.40 \pm 0.01	49.08 \pm 0.12
C1B ϵ R268A/R282A/R283A-ECFP	0.18 \pm 0.01	77.89 \pm 0.74	0.38 \pm 0.01	34.89 \pm 0.49
<i>Converting C1Bϵ into C1Bδ-like</i>				
C1B ϵ K251M/R282H-ECFP	0.17 \pm 0.03	46.47 \pm 1.53	0.20 \pm 0.03	14.53 \pm 1.19

^aPhospholipid vesicles contained 75 mol % POPC, 5 mol % of DOG, 5 mol % OG-PE, and 20 mol % POPA. Binding was measured by protein-to-membrane FRET and data were fitted to a Hill equation. Values are given as mean \pm SE of at least three different experiments.

Table S3. Plasma membrane translocation parameters of PKC ϵ -EGFP in RBL-2H3 cells stimulated with DNP-HSA, DOcPA and/or DOcG.

Stimulation	<i>N</i> cells	M.L. (%)	R_{\max}	$t_{1/2}$ (s)
<i>PKCϵ-EGFP</i>				
2 μ g/ml DNP-HSA ^a	65	92	0.80 \pm 0.04	22 \pm 3
20 μ g/ml DOcPA	28	100	0.81 \pm 0.02	10 \pm 3
10 μ g/ml DOcPA	24	83	0.73 \pm 0.03	13 \pm 2
5 μ g/ml DOcPA	32	34	0.66 \pm 0.02	17 \pm 3
25 μ g/ml DOcG	32	94	0.77 \pm 0.03	6 \pm 2
10 μ g/ml DOcG	26	84	0.70 \pm 0.02	9 \pm 3
5 μ g/ml DOcG	17	41	0.66 \pm 0.02	17 \pm 3
5 μ g/ml DOcPA + 4 μ g/ml DOcG	26	100	0.84 \pm 0.03	9 \pm 2
<i>PKCϵ-EGFP/K251A</i>				
2 μ g/ml DNP-HSA	21	81	0.59 \pm 0.04	22 \pm 6
20 μ g/ml DOcPA	16	87	0.44 \pm 0.04	53 \pm 5
10 μ g/ml DOcPA	18	77	0.28 \pm 0.02	59 \pm 6
5 μ g/ml DOcPA	19	0	---	---
25 μ g/ml DOcG	16	100	0.57 \pm 0.03	12 \pm 3
10 μ g/ml DOcG	34	67	0.36 \pm 0.04	12 \pm 5
5 μ g/ml DOcG	16	37	0.19 \pm 0.02	43 \pm 10
5 μ g/ml DOcPA + 4 μ g/ml DOcG	19	94	0.67 \pm 0.03	13 \pm 3
<i>PKCϵ-EGFP/R268A</i>				
2 μ g/ml DNP-HSA	27	92	0.67 \pm 0.04	48 \pm 6
20 μ g/ml DOcPA	20	85	0.48 \pm 0.02	12 \pm 4
10 μ g/ml DOcPA	19	52	0.22 \pm 0.04	20 \pm 5
5 μ g/ml DOcPA	18	0	---	---
25 μ g/ml DOcG	14	100	0.64 \pm 0.04	10 \pm 2
10 μ g/ml DOcG	22	63	0.46 \pm 0.06	15 \pm 5
5 μ g/ml DOcG	19	26	0.13 \pm 0.02	26 \pm 2
5 μ g/ml DOcPA + 4 μ g/ml DOcG	23	100	0.67 \pm 0.03	21 \pm 6

<i>PKCε-EGFP/R282A/R283A</i>					
2 µg/ml DNP-HSA	25	68	0.39 ± 0.06	58 ± 13	
20 µg/ml DOcPA	12	0	---	---	
25 µg/ml DOcG	17	70	0.31 ± 0.03	19 ± 3	
10 µg/ml DOcG	21	23	0.12 ± 0.01	15 ± 2	
5 µg/ml DOcG	9	0	---	---	
10 µg/ml DOcPA + 4 µg/ml DOcG	11	0	---	---	
20 µg/ml DOcPA + 4 µg/ml DOcG	29	65	0.47 ± 0.08	38 ± 8	
<i>PKCε-EGFP/K251A/R268A/R282A/R283A</i>					
2 µg/ml DNP-HSA	25	0	---	---	
20 µg/ml/ml DOcPA	9	0	---	---	
25 µg/ml DOcG	5	0	---	---	
20 µg/ml DOcPA + 25 µg/ml DOcG	10	0	---	---	

^aRBL2H3 cells were primed with 0.5µg/ml anti-IgE antibody for 16 h and then stimulated with 2µg/ml DNP-HSA. *M.L.* is membrane localization indicates the percentage of cells responding to DNP-HSA, DOcPA and/or DOcG stimulation with plasma membrane translocation. R_{max} is the maximal relative increase in plasma membrane localization of the enzyme. $t_{1/2}$ is the half-time of translocation.

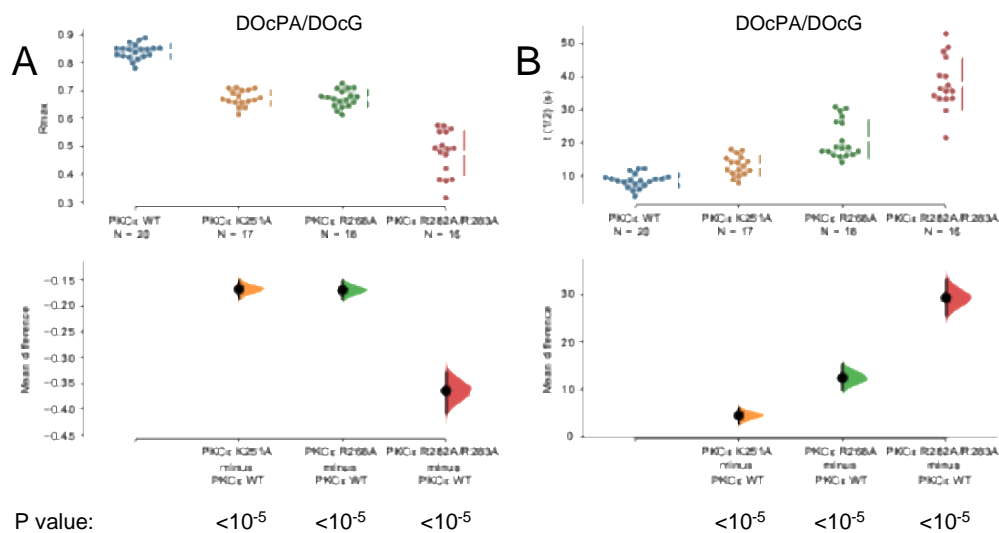


Fig. S2. Plasma membrane localization of PKCε-WT-EGFP in RBL-2H3 cells activated by PA and DAG. Statistical analysis of the R_{max} (A) and Half-time of translocation ($t_{1/2}$) (B) parameters measured when the cells were stimulated with 5 µg/ml DOcPA + 4 µg/ml DOcG (PKCε-WT-EGFP, PKCε-K251A-EGFP and PKCε-R268A-EGFP) and 20 µg/ml DOcPA + 4 µg/ml DOcG DOcPA+DOcG (PKCε-R282A/R283A-EGFP). The mean difference for 3 comparisons against the shared control PKCε-WT-EGFP are shown in the Cumming estimation plots. The raw data are plotted on the upper axes (means are shown as a gap in the right vertical line). On the lower axes, mean differences are plotted as bootstrap sampling distributions (5000). Each mean difference is depicted as a dot and each 95% confidence interval is indicated by the ends of the vertical error bars. Additional permutation test was also applied to confirm these results, the P values to accept/reject the null hypothesis of no differences between the WT and the mutant proteins, are indicated below each comparison (CI 95%).

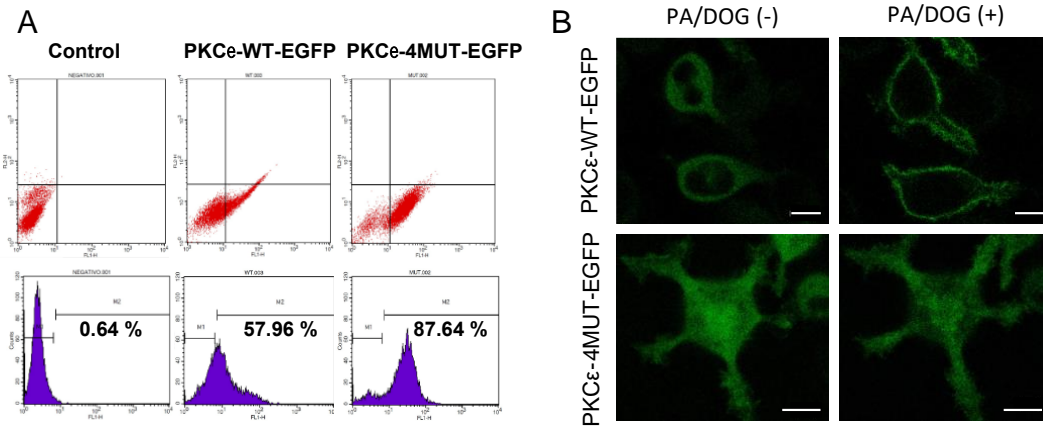


Fig. S3. Stable RBL-2H3 cell lines expressing PKCε-WT-EGFP and PKCε-4MUT-EGFP. (A). Sorting of RBL-2H3 cells was performed for green fluorescent cells expressing PKCε-WT-EGFP and PKCε-4MUT-EGFP and analysing the purity of stable cell lines. Scale bar 10 μm (B). PKCε-WT-EGFP is translocated to the plasma membrane after stimulating with DOcPA+DOcG (5+4 μg/mL, respectively) while PKCε-4MUT-EGFP is not translocated upon similar stimulation.

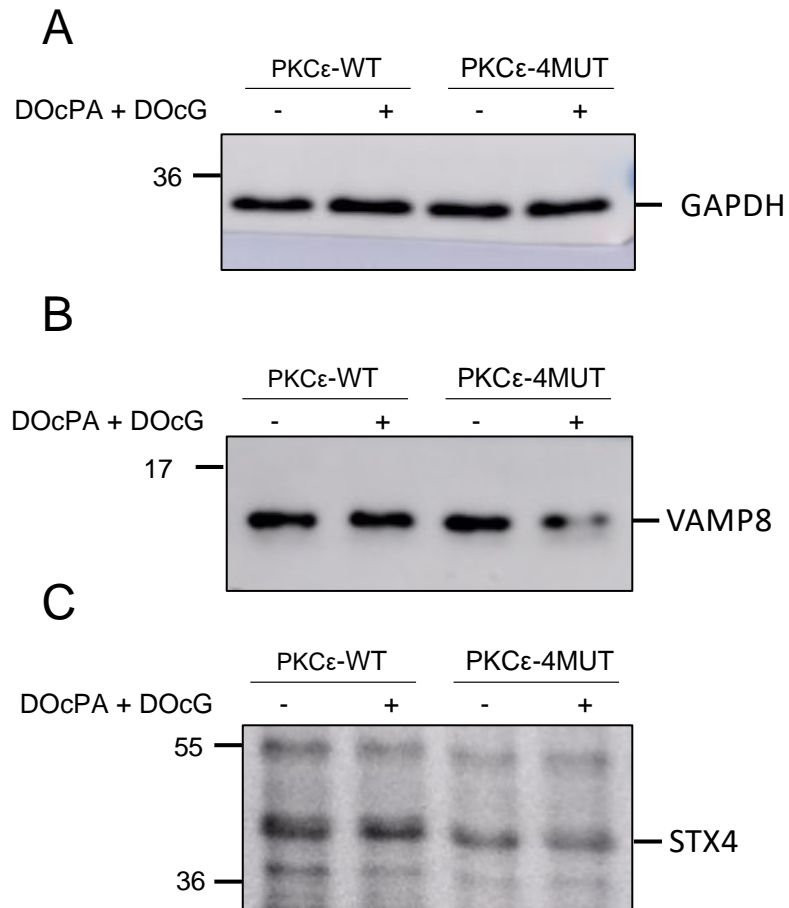


Fig. S4. VAMP8 and STX4 do not have different electrophoretic mobility shifts due to phosphorylation. (A) Western blot against GAPDH of RBL-2H3 transfected cells with PKC ϵ -WT-EGFP and PKC ϵ -4MUT-EGFP stimulated with DOcPA+DOcG. (B) Western blot against VAMP8 of RBL-2H3 transfected cells with PKC ϵ -WT-EGFP and PKC ϵ -4MUT-EGFP stimulated with DOcPA+DOcG. (C) Western blot against STX4 of RBL-2H3 transfected cells with PKC ϵ -WT-EGFP and PKC ϵ -4MUT-EGFP stimulated with DOcPA+DOcG.

Table S4. Phosphorylation sites in the SNARE complex (SNAP23/STX4/VAMP8) determined in PhosphoSitePlus^R 1

PROTEIN	Phosphorylation sites in the coiled-coil structure identified by MS	Phosphorylation sites out of the coiled-coil structure identified by MS
SNAP23 (green)	S20, S23, T24, S160	S5, S95, T102, S109, S110, S120
STX4 (blue)	-----	S15, S35, S117
VAMP8 (red)	S17, T47, T53, S54	-----

¹P. V. Hornbeck *et al.*, 15 years of PhosphoSitePlus®: integrating post-translationally modified sites, disease variants and isoforms. *Nucleic Acids Res* **47**, D433-D441 (2019).